UNIVERSITÀ
DEGLI STUDI
DI TRIESTE

UNIVERSITÀ DEGLI STUDI DI TRIESTE

XXXV CICLO DEL DOTTORATO DI RICERCA IN

NANOTECNOLOGIE

PHD06

Study of soft nanoparticles for drugs delivery

Settore scientifico-disciplinare: **FIS03**

DOTTORANDO / A
FILIPPO COSTA

COORDINATORE
Prof. ALBERTO MORGANTE

SUPERVISORE DI TESI
Dott. STEFANO PRATO

ANNO ACCADEMICO 2021/2022

Per questi porti non saprei tracciare la rotta sulla carta, né fissare la data dell'approdo. Alle volte mi basta uno scorcio che s'apre nel bel mezzo d'un paesaggio incongruo, un affiorare di luci nella nebbia, il dialogo di due passanti che s'icontrano nel viavai, per pensare che partendo di lì metterò assieme pezzo a pezzo la città perfetta, fatta di frammenti mescolati col resto, d'istanti separati da intervalli, di segnali che uno manda e non sa chi li raccoglie.

Italo Calvino

A Sara

Filippo Costa

Contents

Abstract

Interest in nanoparticle-based drug delivery systems (NDDS) has grown in the last decade. The aim of this work is to develop a multispectral nanoimaging system for biomedical studies. This is done in collaboration with A.P.E. Research, which designs and develops imaging and characterization tools. This work is part of the CATHENA (Cancer Therapy by Nanomedicine "POR FESR FVG PROJECT") project. NDDS are systems that allow to transport specific drugs in target tissues. This work focuses on specific NDDS: Solid-Lipid Nanoparticles (SLNPs). These nanoparticles have been extensively studied in solution. My work therefore aims to study the behavior of these nanoparticles once deposited. These analyses will be integrated into the future project for the identification of nanoparticles within sections of biological tissues. Part of this work focus on the study of SLNPs and the dye indocyanine green (ICG) using AFM, Raman spectroscopy, and fluorescence spectroscopy. Those data, with also the morphological characterization of the deposited SLNPs, will be the basis for the multispectral nanoimaging system development.

Estratto

L'interesse per i sistemi di "drug-delivery" a base di nanoparticelle (NDDS) è cresciuto nell'ultimo decennio. Lo scopo di questo lavoro è di sviluppare un sistema di nanoimaging multispettrale per studi biomedici. Questo avviene in collaborazione con A.P.E. Research, che progetta e sviluppa strumenti di imaging e caratterizzazione. Questo lavoro fa parte del progetto CATHENA (Cancer Therapy by Nanomedicine "POR FESR FVG PROJECT"). Gli NDDS sono sistemi che permettono di trasportare farmaci specifici in tessuti target. Questo lavoro si focalizza su specifici NDDS quali nanoparticelle a base lipidica (SLNPs). Queste nanoparticelle sono state abbondantemente studiate in soluzione. Il mio lavoro si propone quindi di studiare il comportamento di queste nanoparticelle una volta depositate su diverse superfici. Queste analisi verranno integrate in un futuro progetto per l'identificazione di nanoparticelle all'interno di sezioni di tessuti biologici. Parte di questo lavoro si concentra quindi sullo studio delle SLNPs e del colorante indocyanine green (ICG) utilizzando AFM, spettroscopia Raman e spettroscopia a fluorescenza. Questo studio servirà a comprendere il comportamento delle nanoparticelle e dell'ICG una volta depositati su un substrato specifico. L'obiettivo è quello di identificare una possibile proprietà che consentirà un facile rilevamento in sistemi complessi quali tessuti bilogici.

Chapter 1

Drugs delivery and solid lipid nanoparticles

1.1 Introduction

Nanotechnology is the manipulation of matter at atomic, molecular, and supramolecular levels that involves the design, fabrication, characterization and application of various nanoscale materials in several key areas. That enable new technological advances, particularly in the field of medicine [1, 2]. Finding new and innovative treatments for cancer is a major problem across the world [3, 4]. Despite a great response, anticancer drugs are administered in high doses which lead to diverse side effects. Some of those effects in normal tissues (e.g., nephrotoxicity, neurotoxicity, cardiotoxicity, etc.) leads to a reduction in drug concentration at the target site, poor accumulation in the tumor, and consequently a reduction in efficacy that can lead to patient relapse [5]. One way to overcome those problems is to reduce the drugs that are administered, delivering them directly on the target tissues or organs with an appropriate final concentration for each cycle of chemotherapy [6]. The development of targeted delivery systems is the ultimate goal in cancer therapy, which has taken the lead in overcoming the multidrug resistance (MDR) problem [5]. Nanotechnology for drug vectoring enables new and more specific platforms for drug targeting and delivery that can reduce toxicity and other side effects and maintain or improve therapeutic index [7]. Drug delivery systems (DDSs) is based on the enhancement of the permeability and retention (EPR) effect 1.1 promoted by angiogenic vessels with defective vasculature and insufficient lymphatic flow around the tumor [2].

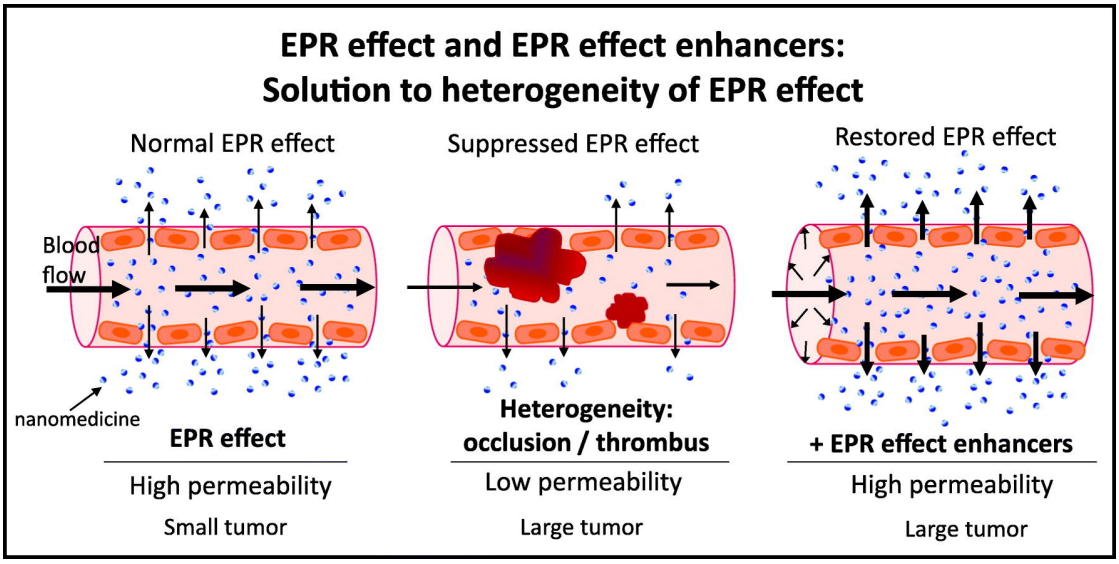

(**1.1**) dynamics of the EPR effect.

In recent decades, various types of nanoparticles have been developed based on different components, including carbon, silica oxides, metal oxides, nanocrystals, lipids, polymers, dendrimers, and quantum dots, as well as an increasing variety of newly developed materials [6]. Nanomaterials offer favorable half-life in blood and physiological behavior with minimal off-target effects, effective excretion from the human body, and minimal or no toxicity to healthy tissues in living organisms [8]. Nanoparticles (NPs) used as DDS have specific sizes, shapes, and surface characteristics. A precise engineering of those characteristics is fundamental on the efficiency of the nano-drug delivery and the control therapeutic efficacy. The dimension of the nanoparticles is related to the permeability and retention (EPR) effect. Small NPs can leak from the normal vasculature (less than $1 - 2nm$) and damage the cells. Also can be easily filtered by kidneys (less than $10nm$ in diameter) [9]. NPs which are to big are likely to be cleared from circulation by phagocytes [10]. A suitable diameter for cancer therapy range from 10 to $100nm$[11]. Three main categories of NPs are based on the composition: Organic NPs, Inorganic NPs and Hybrid NPs. Organic NPs, like liposome, has been widley studied. Modifying the lipid layer structure, can imitate the biophysical characteristics (e.g., mobility and deformation) of living cells [12]. Inorganic NPs on the other hand, have a wide and easily modified surface conjugation chemistry. Lipid-polymer hybrid NPs, which consist of an inner polymeric core and a lipid shell, have been demonstrated to be a promising drug delivery platform in the treatment of several tipe of cancer [13]. This type of NPs combines the high biocompatibility of organic NPs thanks to the lipids structure and the inogranic NPs ability of encapsulating both hydrophilic and hydrophobic drugs. This system can be effectively internalized by

cancer cells and avoids fast clearance by the reticuloendothelial system [14].

1.2 Solid Lipid Nanoparticles

Solid lipid nanoparticles (SLNs) 1.2 are introduced as a delivery system for water-soluble drugs and corrective dynamic drugs. Colloidal particles with size between 10 and 1000 nm are called nanoparticles.

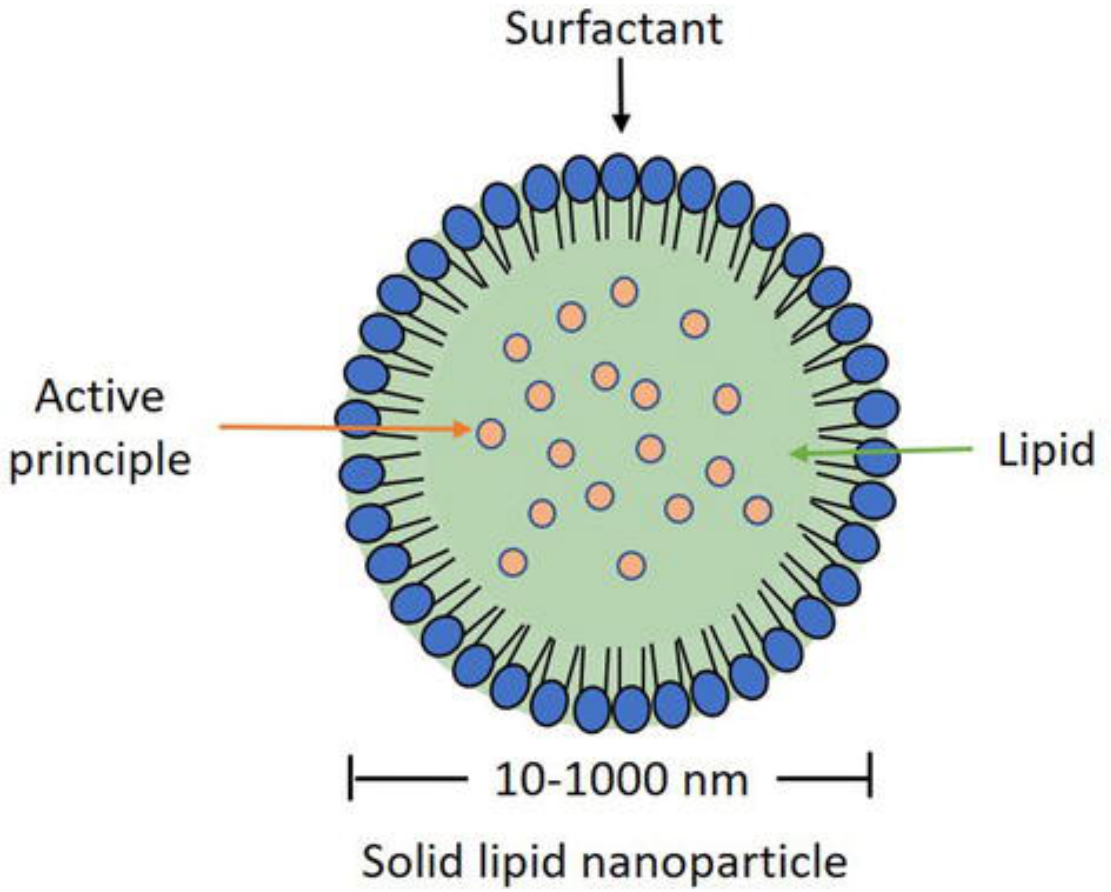

(**1.2**) Solid lipid nanoparticles (SLNs).

They're made of characteristic polymers and are suitable for improving drug transport and reducing lethality [15]. They've emerged as variable substitutes for liposomes as drug carriers. SLNs have interesting properties, such as small size, large surface area, high drug stacking, and interfacial communication of steps, and are interesting because they can improve drug efficacy. Solid lipid nanoparticles (SLNs) are aqueous colloidal dispersions whose matrix consists of solid biodegradable lipids. SLNs combine the advantageous circumstances and keep a strategic

distance from the disadvantages of some colloidal carriers in their class, e.g., physical stability, protection of fused labile drugs, protection of incorporated labile drugs from degradation, controlled release, excellent tolerability SLN formulations for different routes of administration (parenteral, oral, dermal, visual, pulmonary, rectal) have been developed and thoroughly characterized in vitro and in vivo [16].

1.2.1 preparation techniques for lipid particles

Microemulsions are clear or slightly bluish solutions consisting of a lipophilic phase (e.g., lipid), a surfactant and, in most cases, a co-surfactant, and water. The term microemulsion is controversially discussed. Nowadays, microemulsions aren't considered a true emulsion with very fine droplets, but a "critical solution" [17]. Microemulsions exhibit properties of true macroemulsions (e.g., small particle sizes can be measured by laser light scattering) and, at the same time, properties of a true solution (e.g., drugs in a microemulsion have saturation solubility and don't exhibit a partition coefficient as in macroemulsions). The addition of a microemulsion to water causes precipitation of the lipid phase, resulting in fine particles. This effect is exploited in the preparation method for SLN developed by Gasco [18]. To form a microemulsion with a lipid that's solid at room temperature, the microemulsion must be prepared at a temperature above the melting point of the lipid. The lipid (fatty acids and/or glycerides) is melted, a mixture of water, co-surfactant(s) and the surfactant is heated to the same temperature as the lipid and added to the lipid melt with gentle stirring. A transparent, thermodynamically stable system is formed when the compounds are mixed in the correct ratio to form a microemulsion. This microemulsion is then dispersed in a cold aqueous medium ($2 - 3°C$) with gentle mechanical stirring. This ensures that the small size of the particles is due to precipitation and not mechanical stirring [19, 20]. Surfactants and co-surfactants include lecithin, biliary salts, and also alcohols such as butanol [21]. Excipients such as butanol are less favorable from a regulatory point of view. From a technical point of view, the precipitation of lipid particles in water is a dilution of the system, leading to a reduction in the solid content of the SLN dispersion. For some technological operations it is highly desirable to have a high lipid solid content e.g. 30%. An example is the conversion of the SLN dispersion into a dry product (e.g. tablet, pellet) by a granulation process. The SLN dispersion can be used as granules, but in the case of low particle content, too much water must be removed. Large-scale production of SLN by the microemulsion technique also appears to be feasible and is currently being developed at Vectorpharma (Trieste, Italy). The microemulsion is produced in a large temperature-controlled tank and then pumped from this tank to a cold water tank for the precipitation step [22]. Important process parameters during scaling-up are, for example, the temperatures of the microemulsion and the water, but also the temperatures of the

microemulsion and the water medium, as well as the hydrodynamics of the mixing, which should change as little as possible during scaling-up in order to maintain the same product properties.

1.2.2 ICG

The SLNPs are bonded to a special dye base on ICG Indocyanine green (ICG) that is a cyanine dye used in medical diagnostics. It is used for determining cardiac output, hepatic function, liver and gastric blood flow, and for ophthalmic angiography [23] It has a peak spectral absorption at about 800 nm [24]. These infrared frequencies pass trough retinal layers, allowing ICG angiography to image deeper patterns of circulation than fluorescein angiography [25]

Chapter 2

Techniques

2.1 Atomic Force Microscopy (AFM)

Developed by Gerd Binning and coworkers in 1986 AFM exploits the interaction between the atoms present on the edge of an ultra-narrow tip and the sample to obtain morphological informations [26]. The size of the tips is about ten nanometers and the usual tip-surface distance is about $0.1 - 10nm$. P represent the parameter of the interaction between the tip and the sample, a change in the tip-sample distance led to a change of P. Through a *feedback system* (FS) it's possible to keep constant P with a piezo transducer (PT) that controls the tip-sample separation. ΔP signal induces a variation of piezo transducer that brings the value close to P_0. Thanks to this system it's possible to obtain a topography of the sample through a scanning along the x,y value [27]. AFM head is provided of an optical feed-back control system that includes a laser and a four quadrant photodiode sensor and a preamplifier.

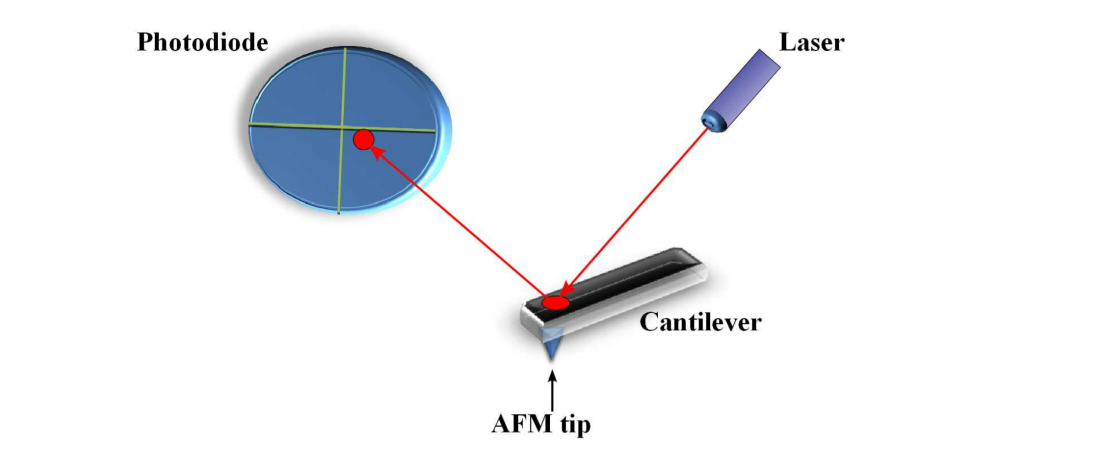

(**2.1**) scheme of AFM optical system for feedback control.

In this control system z-displacement of the cantilever is detected by reflection of a laser beam focused on the top surface of the cantilever (as shown in the scheme). The piezoelectric scanner moves the sample under the tip (or the tip on the sample) in a raster pattern. During the movement the system measure in each point the cantilever bending due to the different interactions (atomic and molecular forces) between the tip and the surface of the sample. In this way we can reconstruct a three-dimensional topography of the sample surface at nanomentric level. AFM system can work in different mode so called Contact AFM mode and Non-contact AFM mode.

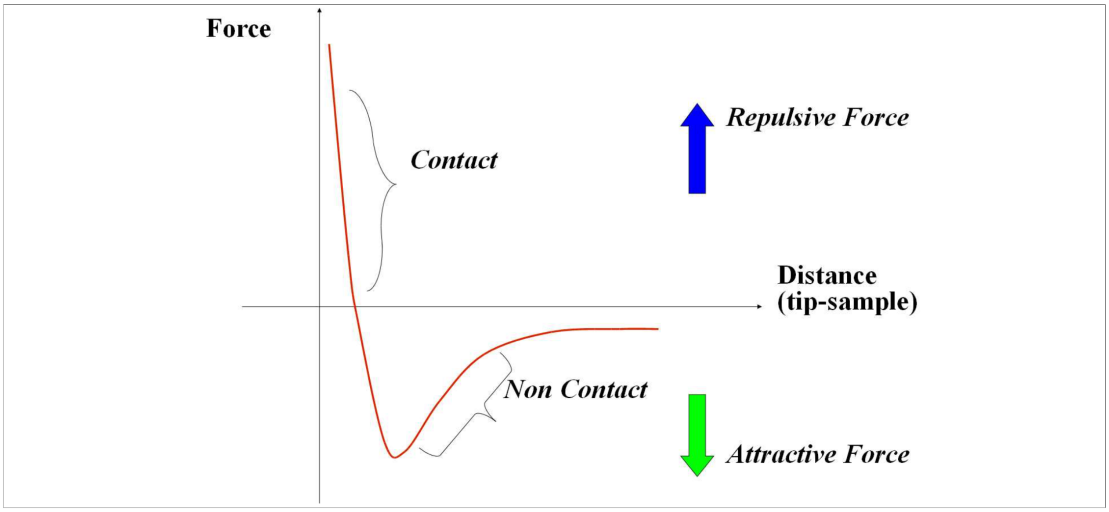

(**2.2**) typical force-distance curve in AFM.

The figure shows the dependence of the inter-atomic force (Van Der Waals

force) upon the tip-sample distance.

2.1.1 Kelvin Probe Microscopy (KPM)

KPM Tool for Kelvin Probe Microscopy (also known as surface potential microscopy) allows to simultaneously obtain a local image of topography and potential. The potential image is obtained from the deflection of cantilever due to the long range electrical forces between the tip and the scanned sample. The potential is usually called as a contact potential difference (CPD). When being in interaction the electrical force is comparable to the Van Der Walls force. To overpass this problem, a combination of DC voltage and AC modulation can be used. In KPM a combination of AC (modulation) and DC (offset) voltage is applied between the tip and the sample, in Non Contact mode. The electrical force is measured through the deflection of cantilever. In comparison with Electrostatic force Microscopy EFM where the voltage is applied to the tip or to the sample, in KPM mode the AC and DC voltage components are always applied between the tip and the sample. Likewise in EFM mode, where the resulting signal is directly proportional to the deflection of the cantilever depending on the applied DC voltage (on the tip OR on the sample), the Kelvin method looks for this DC component and tries to nullify it. In the Kelvin Probe Force Microscopy, the determination of the work function is based on the measurement of the electrostatic forces between the AFM tip and the sample. When the tip and sample are far away (figure 2.3) it means that they are outside the reach of electrostatic forces. At that time the system is in equilibrium and there is no electric field present, although the Fermi levels of the tip/sample are different.

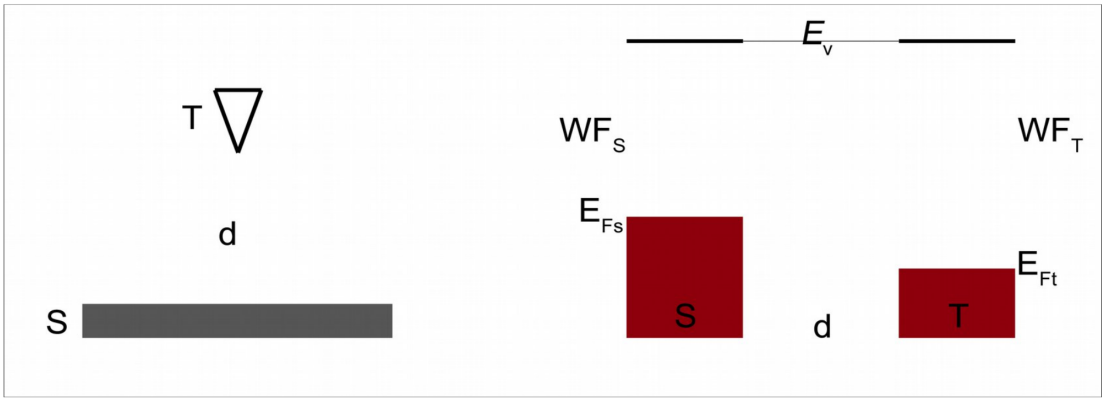

(**2.3**) Large distance between tip (T)/sample (S) and energy levels.

When the tip is brought to a closer distance (figure 2.4) a new equilibrium state must be established – Fermi levels tend to line up – and tunneling occurs.

Until the new equilibrium state is settled, tunneling take its place and a negative charge for example is generated on the tip. At the same time the opposite charge (positive) is generated on the sample. From the energy point of view, Fermi levels are now lined-up but because we are in the non-contact regime, the DC voltage between the tip and sample is generated. This potential ($V_{(DCP)}$) is the potential which drives the force between tip-sample.

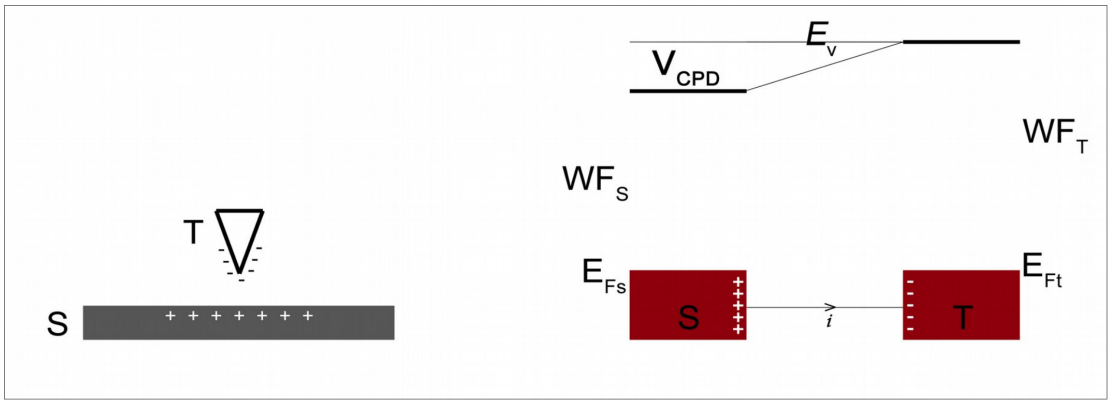

(**2.4**) Electronic contact between tip (T)/sample (S), Fermi levels are equalized.

Now the vacuum energy levels of tip/sample are not the same any more. In order to level it, a DC voltage of the opposite amplitude between the tip-sample must be applied (figure 5.6). With that, the effect of the surface charge above the scanning area is eliminated and the difference between the work functions of tip/sample can be now measured directly.

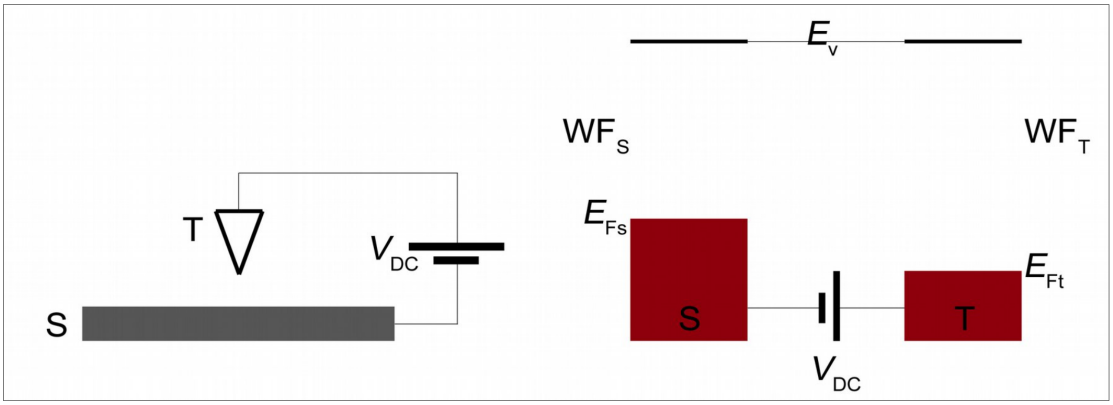

(**2.5**) Electronic contact between tip (T)/sample (S), a DC voltage applied in order to nullify $V_{(DCP)}/electrostatic force$.

In case of knowing the work function of the tip, the work function of the measured material can be calculated.

2.2 Raman Scanning

2.2.1 introduction

Vibrational spectroscopy is widely used to determine molecular structure and plays a central role in many fields, from basic chemistry to materials engineering. Among these techniques, Raman spectroscopy is now indispensable for the study of nanostructured materials and biological systems under in situ and in vivo conditions. Moreover, amplification allows very small quantities to be analyzed (in certain cases down to the single-molecule level). Since each atomic vibration has a characteristic position and intensity, detailed information about molecular structure can be obtained. Both the position and the intensity are influenced by the chemical environment, i.e. chemical bonds, inter- and intramolecular forces.

Raman Scattering

Raman spectra have a different origin than infrared absorption (IR); an inelastic scattering process is responsible for the appearance of the vibrational bands. In IR spectroscopy, the radiation is absorbed by the available vibrational states $(E_1, E_2, E_3, ...E_N)$, which means that the photon energy must match the energy difference between two available states. Therefore, $E_N - E_1 = h\nu$, where h is Planck's constant. In Raman spectroscopy, a molecule can scatter a monochromatic (ν_0) radiation. Usually Raman experiments use lasers with photon energies from the UV to the near IR range. Elastic scattering is called Rayleigh scattering and is much more intense than inelastic Raman scattering (about 10^{-8} less than the intensity of the incident radiation). The Raman spectrum appears at a wavelength (λ_o) slightly higher or lower than the incident radiation [28, 29, 30, 31, 32]

Therefore, this scattering process can be represented as a perturbation of the molecule by the incident photon, whose *eigenstate* can be described as a linear combination of the *stationary-state* (or *time-independent*) wave functions of the molecule. The pertubated states of the molecule are called "virtual" because they aren't states from the stationary state (*eigenstates*). The photon released when the molecule returns to the ground electronic state usually has the same energy as the incident photon, which characterizes Rayleigh scattering. Raman scattering, which contains vibrational information, can be illustrated in the energy diagram in fig.2.6. 1. The photon energy $(\nu_0 - \nu_m)$ appears in the region of the spectrum called Stokes region; moreover, the photons with energy $(\nu_0 + \nu_m)$ appear in the anti-Stokes region. The bands observed in the anti-Stokes region are less intense than those in the Stokes region because of the differences in the population according

to the *Maxwell-Boltzmann* distribution, so the bands from the Stokes region are more intense than the anti-Stokes Raman region [33, 34, 35].

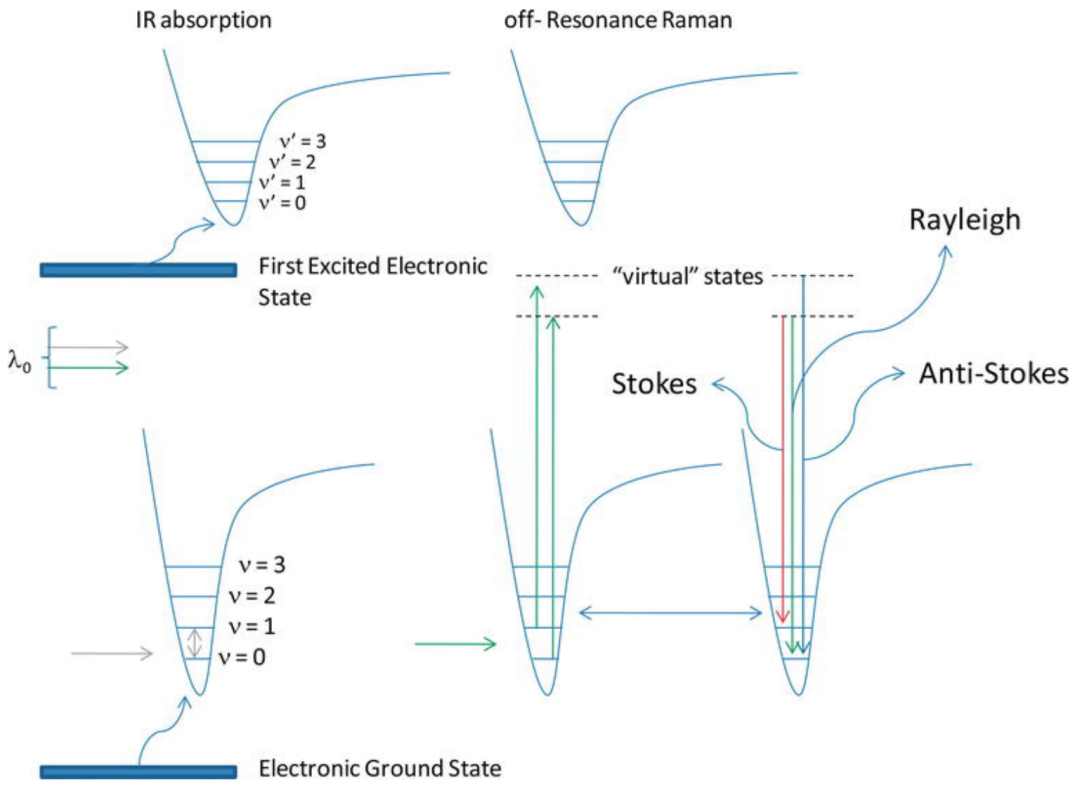

(**2.6**) Schematic representation of the energy diagrams for a diatomic molecule. The figure represents the IR absorption and the Raman scattering in off-resonance or normal condition.

A vibration (vibrational coordinate ϱ) is Raman active if the polarizability (α) (or induced dipolar momentum) of the molecule is changed; it's described as:

$$\frac{\delta\alpha}{\delta\varrho} \neq \emptyset \tag{2.1}$$

Since the nature of the Raman effect is physically different from that of the infrared effect, the selection rules are also different, resulting in different spectra. In fact, these two techniques complement each other and are combined in many cases for structural elucidation.

Nowadays, Raman spectra can be collected with instruments that have a microscope (see Fig. 2.6). The laser line is introduced into the sample on the microscope

stage. More sophisticated microscopes can be connected to the Raman spectrograph, such as STM or AFM microscopes and also electron microscopes [36, 37]. The scattered light is collected at 180°, and a high-efficiency notch filter must be used to block out the incident radiation and also the elastic scattering, since the Raman signal is very small (typically a cross-section factor of 10^{-6} to 10^{-12} of incident radiation). Raman microscopy is a nondestructive technique and typically requires no sample preparation, and measurements can be made in aqueous solution (which isn't possible with conventional IR spectroscopy). The main advantage is the ability to focus the laser on a very small part of the sample (about 1 μm or smaller). The high lateral resolution and depth of focus (on the order of a few micrometers) are very useful, for example, in the study of nanostructured materials and in situ measurements [38, 39, 40, 41, 42].

2.3 Scanning Near-fied Optical Microscopy (SNOM)

The spatial resolution of components in biological systems is a classical biophysical problem. Most imaging techniques currently in use are fundamentally limited by the wavelength of the radiation. This method allows non-destructive imaging of surfaces in their natural environment The resolution limits for this technique lie between the extremes of optical microscopy ($250nm$) and the fluorescence energy transfer method ($\simeq 4nm$ to $\simeq 8nm$). When using visible wavelengths, a conservative estimate of resolution is $50nm$. Analysis of individual macro molecules using near-field optics shown that the orientation of the molecular transition dipole moments can be determined by the correct interpretation of the characteristic near-field excitation patterns produced by the presence of both laterally and longitudinally polarized electric fields near the aperture edge. Local optical field distributions observed was $45nm$ FWHM. The confined optical field is sufficient to discriminate molecules at distances less than $10nm$, compared to $> 40nm$ for far-field.[43].
The basic principle of the SNOM concept is shown in Fig. 2.7, in which visible light is normally incident on a conducting screen with a small aperture (below the wavelength). Since the screen is completely opaque, radiation passing through the aperture into the region beyond the screen is initially collimated to the size of the aperture rather than to the wavelength of the radiation used. This occurs in the near-field region. Eventually, the effect of diffraction is noticeable by a significant divergence of the radiation, resulting in a pattern that no longer reflects the geometric image of the aperture. [44].

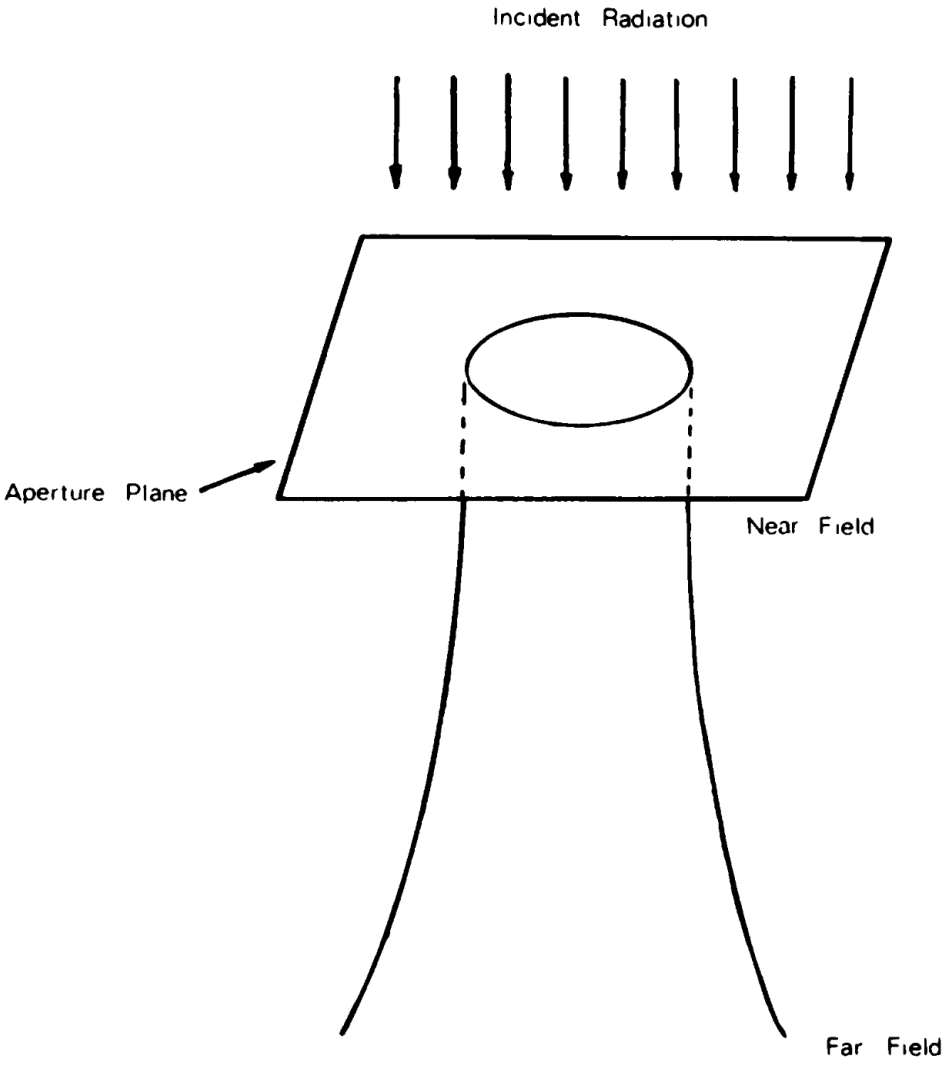

(**2.7**) Schematic representation showing the collimation of radiation emanating from a subwavelength aperture.

To apply the collimation phenomenon, an object, such as a cell membrane, is placed in the near-field region relative to an aperture. In this case, the aperture acts as a light source whose size isn't limited by the geometric optics. The light source can be scanned across the object and the captured light can be used to produce a high-resolution image. Since resolution depends on the size of the aperture rather than the wavelength, it should be possible to achieve a resolution of $50nm$ or more if an aperture with a smaller diameter is used. These are the essential features of the SNOM technique, which can be applied in air with non-ionizing visible

radiation and can be used to image macromolecular assemblies in functioning biological systems at high resolution.

2.3.1 Resolution Limits

Spatial resolution is complex subject. Lateral resolution is related to several factors (i.e. the pixel size of the image and the radius of the tip).

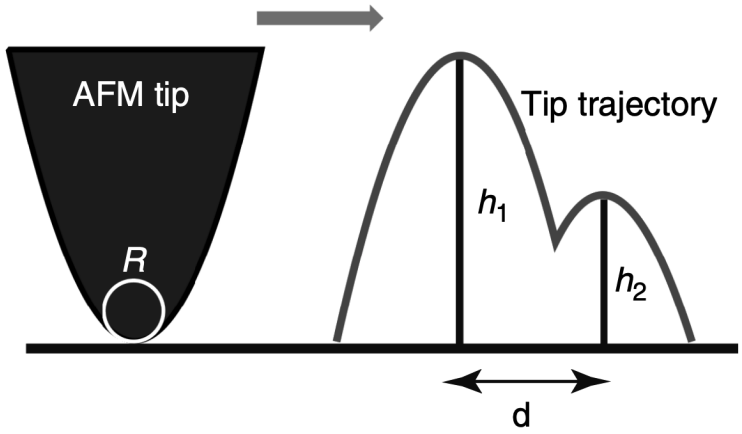

(**2.8**) Dimensions and shape of the tip and on the relative height of two objects.

It is usually defined as the ability to distinguish a single point. A criteria was given by Fabry and Perot: A peak is resolved if it is at least separated by a FWHM from another one [45].

Chapter 3

Analysis and Characterizations

3.1 Introduction

To define the experimental setup, I decided to characterize the SLNPs both morphologically and spectroscopically. I assumed that changes in the environment will result in both deformations and shifts in fluorescence. The main features studied will be:

- **Morphological**: I performed AFM, KPM and EFM analysis. Differently from PCS analysis the particles will be no longer in solution. The deformation of the SLNPs once they have settled on a surface has been investigated. The interactions of the surface with the substrate and the absence of a liquid medium in the environment are clearly significant differences.

- **Spectroscopy**: I decided to study two main features, fluorescence and possible Raman fingerprints. I want to identify specific features for detection in the abundance of the biological environment. Fluorescence is also related to the ICG dye. Literature is mainly concerned with the solution system in the case of both SLNPs and ICG. Analyses will examine these properties after deposition on different substrate.

3.2 AFM, KPM and EFM

The first analysis concerned the morphological characterization of the solid-lipid nanoparticles. I decided to use AFM and KPM techniques to analyze the nanoparticles deposited on a substrate. I developed a method to obtain images in which the SLNPs appear separately.

3.2.1 Substrates

I tested different substrates with the aim to understand how to use the technique in the best way. The goal was to obtain non-aggregated SLNPs. Another important property I considered was the interaction between the substrate and the SLNPs to reduce deformation effects. I've performed several preliminary tests to find possible influences on further analysis with the SLNPs. The following are the substrate I choose for the analysis:

- Soda-Lime Glass
- Silicon
- Highly oriented pyrolytic graphite (HOPG)
- poly(3,4-ethylenedioxythiophene) polystyrene sulfonate (PEDOT)
- Soda-Lime Glass
- Gold substrates for STM applications

Soda-Lime Glass is a transparent substrate suitable also for transmission SNOM imaging. I used a particular substrate made by gold pin on silicon for the fluorescence and Raman analysis so I decided to try to characterize the SLNPs both on silicon ad on gold substrates. I also tested SLNPs on HOPG and PEDOT due to their conductivity for KPM analysis 3.3c.

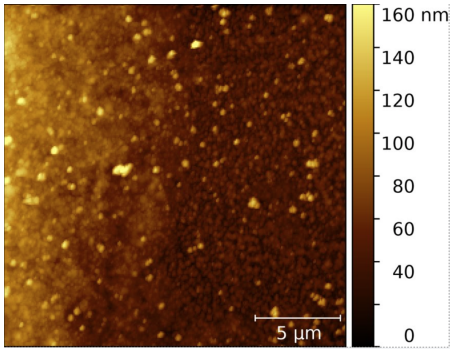

(a) AFM PEDOT topography image.

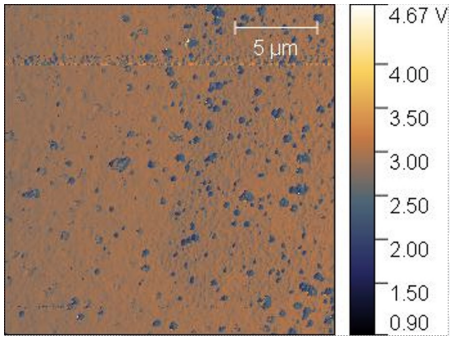

(b) AFM PEDOT phase image.

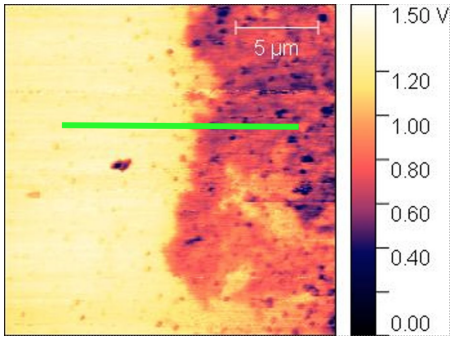

(c) AFM PEDOT KPM image.

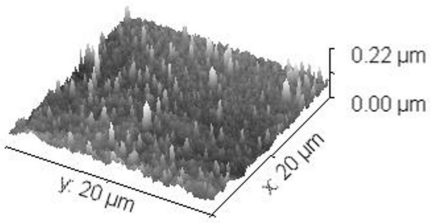

(d) AFM PEDOT topography 3D image.

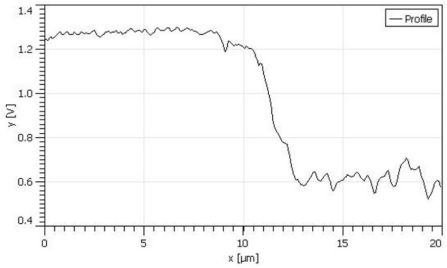

(e) AFM PEDOT profile graph.

(**3.1**) AFM PEDOT substrate analysis.

3.2.2 Sample preparation

I performed various tests related to the substrate and the SLNPs solution to determine the best setup for AFM analysis:

Initial deposition

The starting solution for the deposition of SLNPs was based on glucose solution. The nanoparticles were deposited by a drop-casting method. After a drying phase

at room temperature, various analysis were performed on the bulk and on the edge of drop. In this first phase, I wasn't able to distinguish individual nanoparticles. This was related to the high density of the solution. At the edge I was able to detect the presence of glucose crystals which compromise the analysis.

Diluitions

From the original solution based on glucose, I moved to the solution of SLNPs in H_2O. Again, the solution was too dense to distinguish individual nanoparticles. I tried different substrates to see if a more hydrophobic substrate would lead to greater separation of SLNPs at the edge of the drop. I decided to proceed with multiple dilutions to reduce the concentration of SNLPs on the deposited drop. Here is the dilution from the initial solution:

- $1 \cdot 10^{-1}$
- $1 \cdot 10^{-2}$
- $1 \cdot 10^{-3}$
- $1 \cdot 10^{-4}$
- $1 \cdot 10^{-5}$

This step required special attention to avoid the disgregation of SLNPs during the process.

3.3 Gold deposition

Using a PVD system, I decided to deposit a thin gold film on different substrates. The goal was to investigate future applications for transparent substrates. I chose gold because it is less susceptible to oxidation. The idea was to use SPM techniques that offer the possibility to detect the transmission signal when the substrate is covered by a thin gold layer. I wanted to investigate the influence of the surface structure of the new substrates on the SLNPs after drying. Another test I performed was the deposition of a thin film of gold on the nanoparticles once deposited. The goal was to analyze the nanoparticles through STM.

3.4 Raman Fingerprints

In this section, I investigate the Raman fingerprints of SLNPs and the ICG dye. Those fingerprints will allow us to distinguish the SLNPs in the abundance of

biological media. Using the Scanning MicroRaman system, both SLNPs and ICG deposited on different substrate were analyzed.

3.4.1 Substrates

I decided to use two different substrates:

- Soda-lime Glass

- Gold pin on Silicon

3.4.2 Soda-lime Glass

Most histological section are prepared on soda-lime glass. I decided to study this substrate to get closer to the future conditions under which both nanoparticles and ICG will be analysed. Firstly, I investigate the differences in the spectrum between two conditions, immediately after deposition (solvent present) and after drying (solvent evaporated) 3.2c. Drying step consist in leaving the solvent to evaporate at room temperature. Another analysis was carried out with the dried sample. I want to investigate the influence of the thickness and the way of crystallisation of the ICG in different parts of the deposited drop.

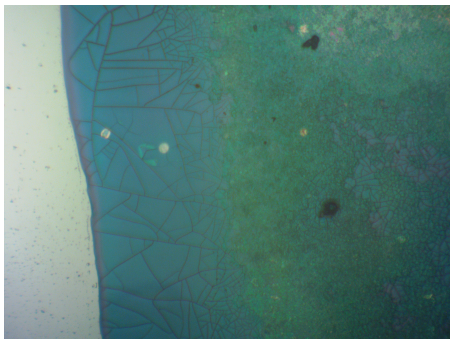

(a) Optical microscopy image: *Objective:* $20x$, *Field of view*$359,5um$.

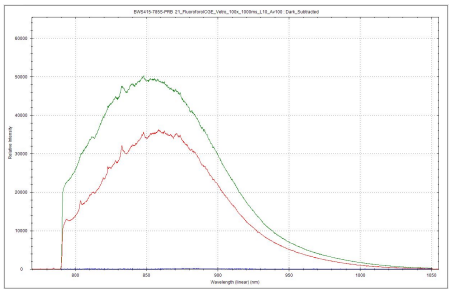

(b) Raman spectra on bulk (*Green*), on the edge (*Red*) and on the glass (*blue*): *Laser Power* $(20mW)$, λ : $(785nm)$, *Exposure Time*: $(1000ms)$ *Objective*: $(50x)$.

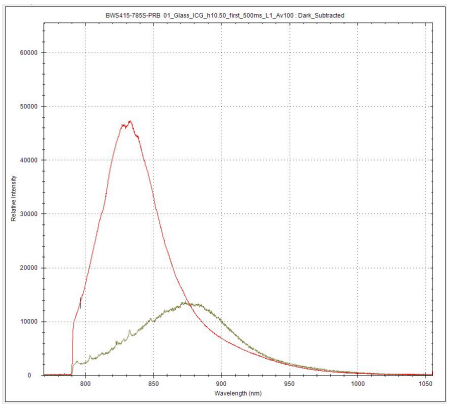

(c) Raman spectra right after deposition (*Green*) and once dried (*Red*): *Laser Power* $(20mW)$, λ : $(785nm)$, *Exposure Time*: $(1000ms)$ *Objective*: $(50x)$.

(**3.2**) ICG analysis on Soda-lime Glass.

Figure 3.2c shows the spectra collected for ICG directly after deposition and after drying. After the evaporation of the solvent the ICG is distributed on the surface and the amount of ICG present in the laser section during the analysis were less than the one not dried, this led to a decrease in the fluorescence signal. The second analysis (Fig. 3.2b) shows the influence of the layer thickness. The technique I used caused the substrate to bleach during the analysis, so increasing the thickness of the substrate led to an increase in the collected signal.

3.4.3 Gold pin on silicon

Another substrate I decided to use was a gold pin deposited on silicon. The idea was to investigate the influence of the plasmon resonance on the amplification of the Raman signal for further studies. In a first step, I analysed the substrate with SEM technique (Fig.: 3.3b). Thanks to the scanning MicroRaman system, I was able to create a hyperspectral map showing the distribution of the analite on the surface (fig.: 3.3d).

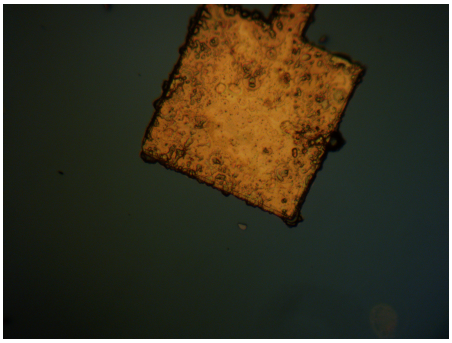

(a) Optical microscopy image: *Objective:* $20x$, *Field of view*$359,5um$

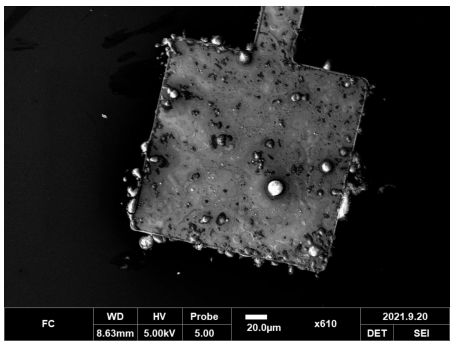

(b) SEM image.

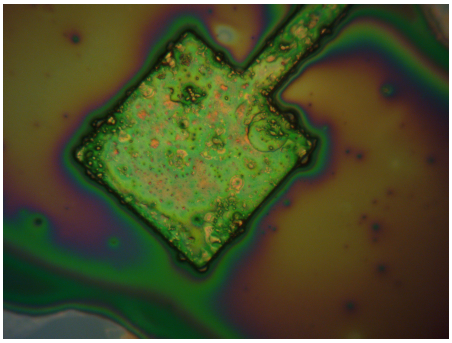

(c) Optical microscopy image after deposition of ICG solution: : *Objective:* $20x$, *Field of view*$359,5um$

(d) Raman-Scanning map: *Laser Power* $(2mW)$, λ : $(785nm)$, *Exposure Time*: $(10ms)$ *Objective*: $(100x)$, *Scan dimension*: $2000x2000um$

(**3.3**) ICG Raman analysis.

The colour scale is proportional to the integral of the single spectrum recorded in the pixel. Is possible to see an increase in the signal for the ICG on top of the

gold pin and at the edge of the drop. The increase in the signal at the edge is due to the greater amount of ICG present.

Vacuum treatment

Because of its influence on the analysis, I added a vacuum treatment step during the sample preparation. Vacuum treatment brings the sample to a pressure of less than $7.9.10 - 2torr$. This step also shortens the time needed to dry the sample.

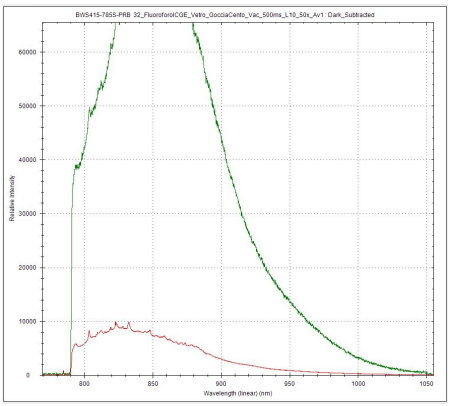

(a) Raman spectra on ICG immediately after deposition (*Green*) and after vacuum treatment(*Red*): *Laser Power* $(20mW)$, λ : $(785nm)$, *Exposure Time*: $(1000ms)$ *Objective*: $(50x)$.

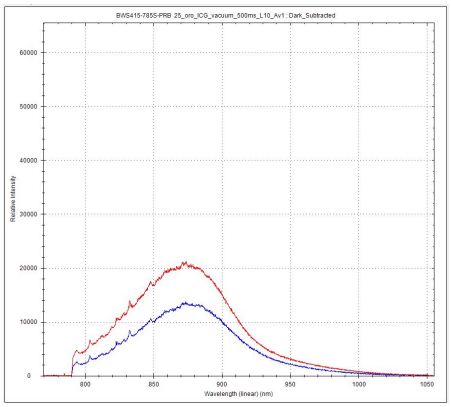

(b) Raman spectra of ICG dried at room pressure (*Red*) and after vacuum treatment(*Blue*): *Laser Power* $(20mW)$, λ : $(785nm)$, *Exposure Time*: $(1000ms)$ *Objective*: $(50x)$.

(**3.4**) ICG vacuum and room pressure analysis on Soda-lime Glass.

Chapter 4

Customization, upgrade and development

In this chapter will be discussed the development of the set-up from two instrument provided by A.P.E. Research.

4.1 Upgrade of the A.P.E. Research SNOM set-up

The aim of this work is to develop a multispectral nanoimaging system for biomedical studies. Specifically I want to develop a tool that can perform imaging on various substrates detecting the SLNPs. The data discussed in Chapter 3 suggests that the properties of nanoparticles should I will rely on for the system development are the following:

- SLNPs fluorescence
- ICG Raman Fingerprints

I decided to use scanning near-field optical microscopy (SNOM) due to the strong fluorescence shown by both ICG and SLNPs.

4.1.1 A.P.E.Research TriA-SNOM structures

A.P.E.Research's TriA-SNOM structure collects information in both reflection and transmission (Fig: 4.2b). SNOM optical reflection and optical transmission signals are detected with two photomultipliers PMT (R74000, Hamamatsu Photonics KK Hamamatsu city, Japan). The SNOM probe 4.1 consists of an aluminium-coated pulled optical fibre with a nominal tip aperture of $50nm$ (Lovalite, Besancon, France).

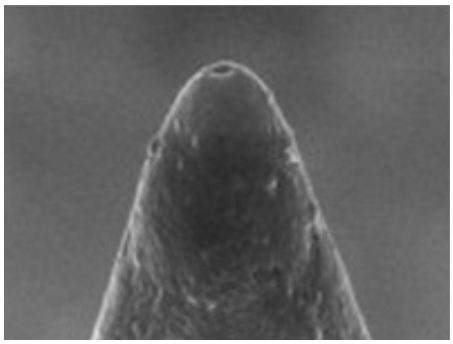

(a) SEM image of the tip.

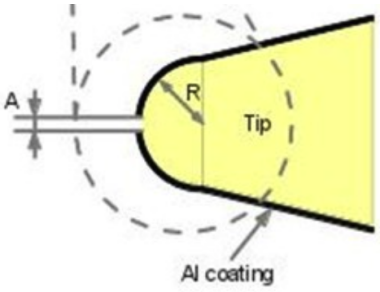

(b) Scheme of optical fiber and the aperture.

(**4.1**) Lovalite SNOM probe.

Two optical vision systems are integrated within the SNOM head to control the probe position and select the scan area. An upper optical vision system is used to monitor probe approach to the sample, while one transmission camera (with interchangeable achromatic objectives) is utilized for a bottom view of the sample. To provide an absolute positioning, the SNOM is equipped with a flexure scanning stage with a maximum x-y scan area of $100\mu m \times 100\mu m$ and z-scan range of $10\mu m$ (high voltage mode), with strain gauge sensors. To operate the fluorescence SNOM, I work with the following components:

- laser source
- Signal collection system

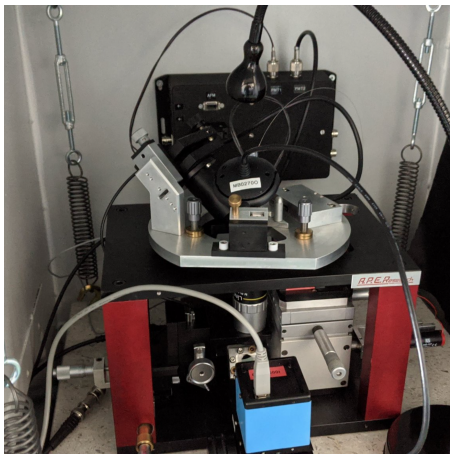

(a) photo of the setup.

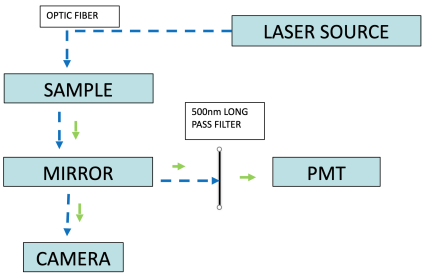

(b) SNOM scheme.

(**4.2**) A.P.E.Research TriA-SNOM structure.

4.1.2 laser source upgrade

Although a certain fluorescence has been identified for the deposited SLNPs, this does not prevent variations related to the environment surrounding the SLNPs. In order to be able to follow possible shifts, I decided to implement the tool by expanding the spectrum of work. A modulation box has been created to regulate the power of different lasers. I want to be able, in a short time, to differentiate the source without having to substantially change the setup and then allow measurements in succession with different wavelengths. This system allows to independently modulate each laser which are directed to the SNOM fiber.

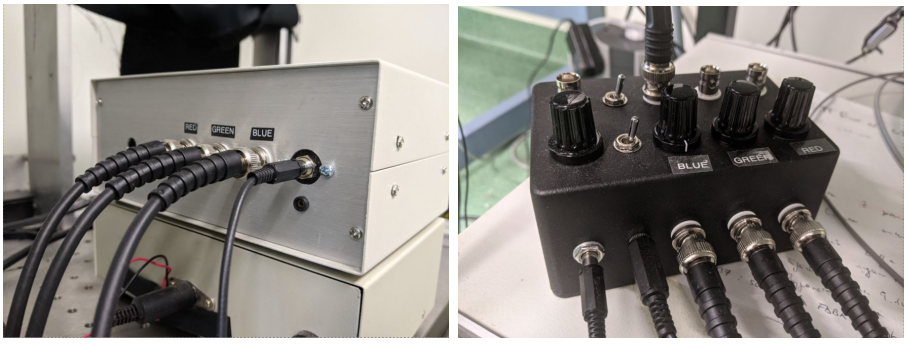

(a) Laser box (b) regulator

(**4.3**) Laser system.

To control the power of each laser in the new trichrome (RGB) design, a junction box with special electronics (fig. 4.3b) was developed to control the power (via PWM) and modulate the signal amplitude (via sine wave) with frequencies from 1 Hz to 1 kHz. The available wavelength is as follows:

- Red = 650 nm
- Green = 532 nm
- Blue = 445 nm

Optical fibre analysis

I performed an analysis on the SNOM fibre to rule out a possible influence in future fluorescence analyses. I replaced the SNOM photomultiplier tube (PMT) with a spectrometer to analyse the wavelength of the beam from the optical fibre. Thanks to the Ocean Optics Flame ® spectrometer I was able to prove that the fluorescence don't contribute to the image in a way that could affect the results.

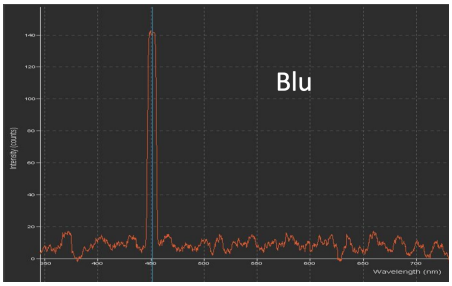

(a) Analysis results for $= 445nm$.

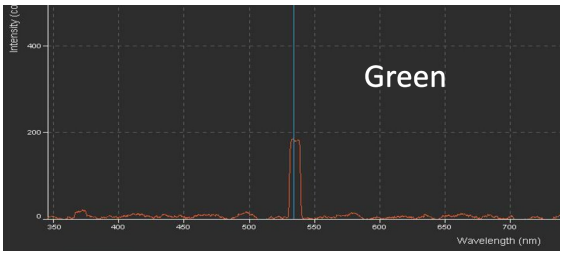

(b) Analysis results for $= 532nm$.

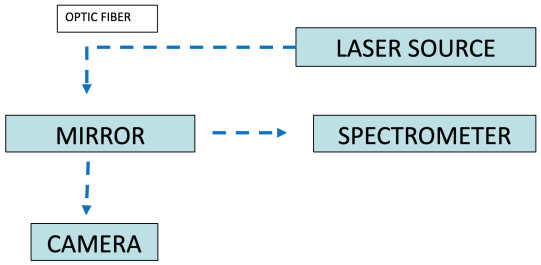

(c) Setup scheme.

(**4.4**) Fiber fluorescence analysis.

As can be seen in Figure 4.4a and Figure 4.4b, the signal is defined around a specific wavelength. This rules out the possibility that the signal comes from the fluorescence of the optical fibre.

4.1.3 Signal collection system upgrade

The second upgrade I've made involves the design and development of a special optical filter system. This system allows to see the possible fluorescence of the sample through the instrument's inverted microscope. With this microscope, the operator can use a specific magnification to understand and decide on which part of the sample start the analysis. Thanks to this filter system, it's possible to focus the analysis directly on each fluorescence point in the sample. The filter in this new system are the following (the filters are changed depending on the wavelength used):

- **BandPass filter**: This filter is placed in front of the white led for the inverted microscope illumination. It serves to filter the white led light to a certain wavelength.
- **LongPass filter**: This filter attenuates shorter wavelengths and transmits longer wavelengths. This serves for the fluorescence analysis.

A special device has been built to switch between PMT and the inverted microscope camera. This makes it possible to work in two different phases. In the first phase, the samples are illuminated with monochromatic light thanks to the inverted microscope. The reflected rays are captured by the CCD camera after passing through the long-pass filter. The images generated are associated with the fluorescence of the sample. The operator can then detect the presence of certain fluorophores in the samples. The second phase concerns SNOM analysis. The operator switches from the camera to the PMT. In this phase, the sample is illuminated by the optical fibre and the transmission signal passing through the long pass filter is detected by the PMT.

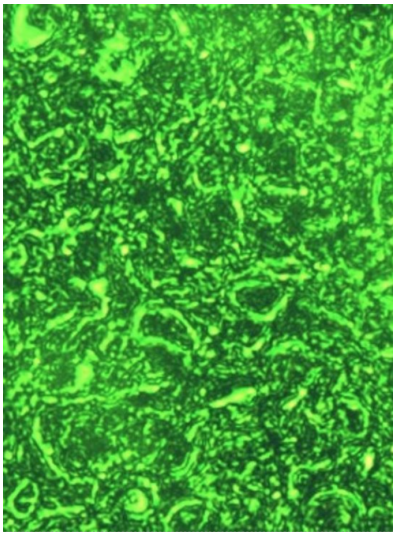

(a) Optical image from A.P.E.Research TriA-SNOM set-up.

(b) Fluorescence optical image from A.P.E.Research TriA-SNOM set-up.

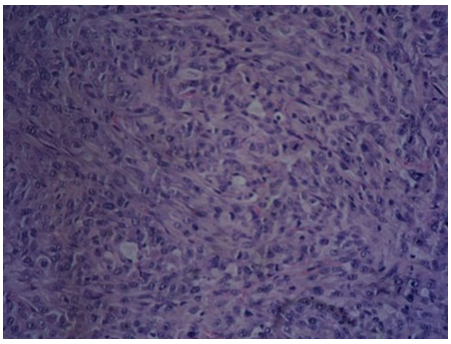

(c) Optical microscopy image: *Objective:* $20x$, *Field of view*$359,5um$.

(**4.5**) A.P.E.Research TriA-SNOM optical collection section for fluorescence analysis.

4.2 SPM setup for the analysis of samples with coverslip

In my research work, I collaborate with the C.R.O. (Oncological Research Centre) in Aviano. Most of the samples provided by the C.R.O. in Aviano are prepared using standard methods that involve the presence of coverslip. In order to perform fluorescence analysis on these samples and test the fluorescence capabilities of the

instrument, I decided to modify the SNOM instrument. As a first experiment, I changed the optical fibre. Instead of the conventional glass fibre tip, I worked with a special glass fibre that ends with a microlens. With this microlens, I was able to focus the beam a few microns away from the tip. It's important to emphasise that the phenomenon exploited by this technique is no longer the near field. Unfortunately, the working distance was not sufficient to overcome the coverslip. So I developed an optical scanning system. This system uses most of the components of A.P.E.Research's TriA-SNOM (i.e. the laser source, signal collection system, scanner stage, etc.) to produce images by focusing the laser beam using a lens under the coverslip. The image is generated pixel by pixel through multiple analyses by moving the sample using the scanner stage. The light is focused on the sample and the reflection and transmission signal is detected by a PMT.

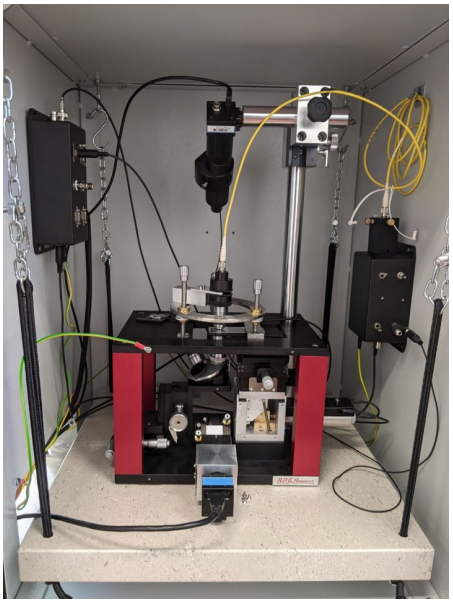

(a) image of the setup.

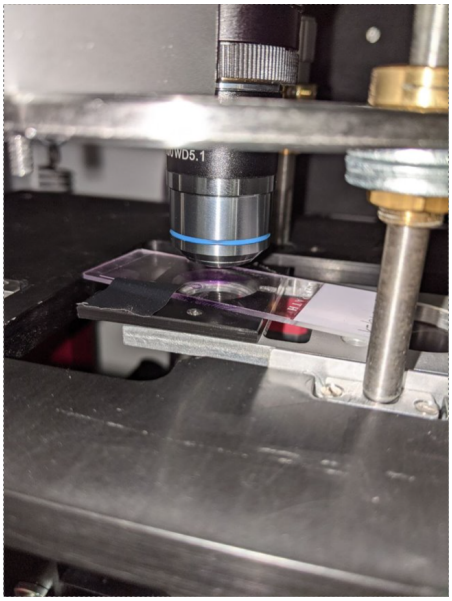

(b) image of the objective.

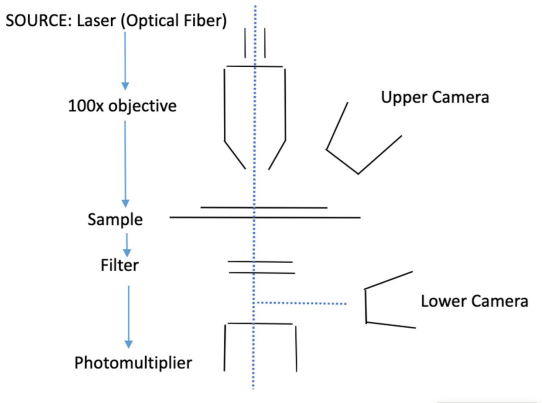

(c) Setup scheme.

(**4.6**) SPM fluorescence setup.

The resolution of the technique is affected by the Abbey limit:

$$d = \frac{\lambda}{n \cdot sin(\alpha)} \tag{4.1}$$

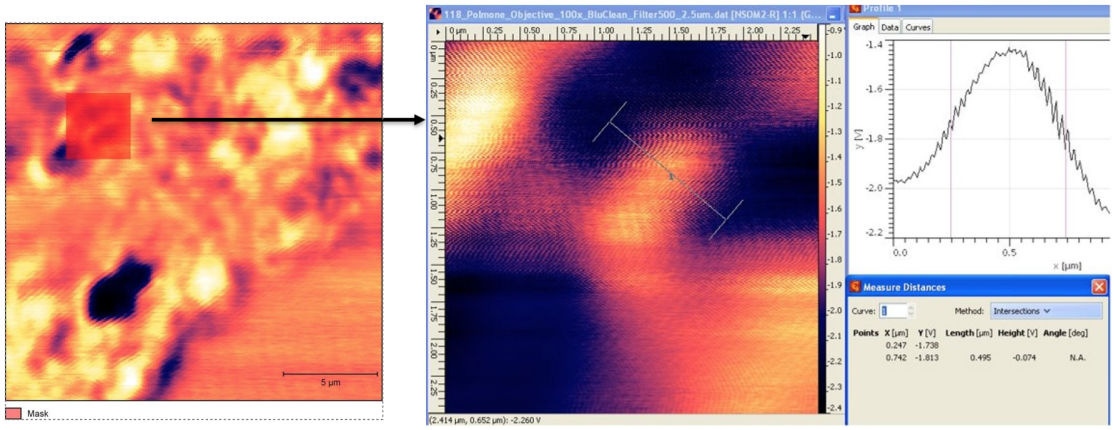

(**4.7**) Smallest object we were able to see.

Samples from the C.R.O., the ICGEB Institute and the CNR laboratories were analysed. All samples were histological sections with fluorophores.

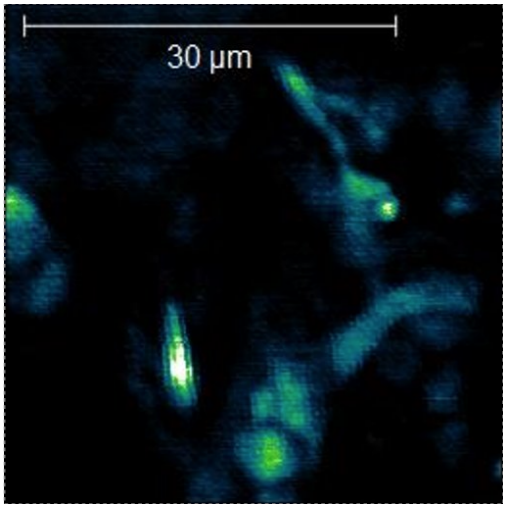

(a) SPM map:λ: ($445nm$), *Filter*: ($500nm$) *Objective*: ($100x$), *Scan dimension*: $40x40um$.

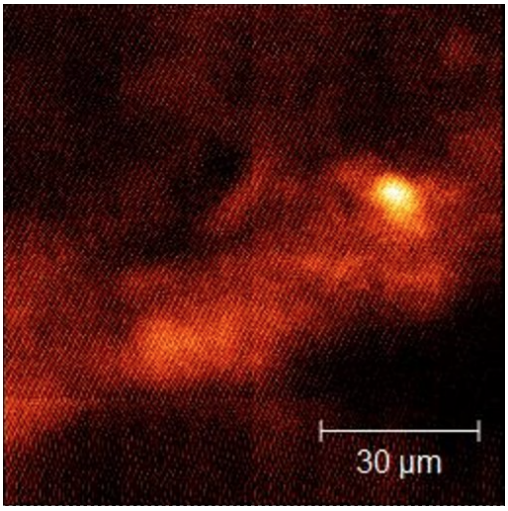

(b) SPM map:λ: ($550nm$), *Filter*: ($600nm$) *Objective*: ($100x$), *Scan dimension*: $95x95um$.

(**4.8**) Tissue sample of lung with different fluorophores from I.C.G.E.B. institute.

4.3 Upgrading the A.P.E. Scanning MicroRaman Instrument

The Scanning MicroRaman consists of a Raman spectroscopy instrument that can produce hyperspectral images by moving the sample using a scanning stage. Each pixel of the image is associated with the integral of the recorded spectrum. To increase the resolution of the device, I replaced the laser source with one able to produce a smaller spot. Reducing the size of the spot makes it possible to record spectra of smaller areas. One problem was that the measurement provided less information due to the smaller amount of light from the laser. To solve this problem, the acquisition time had to be changed by around one order of magnitude per spectra meaning a greater increase in the time for collect the overall map. Despite the improvements, I had to increase the exposure time. This led to an increase of the time needed to create each image.

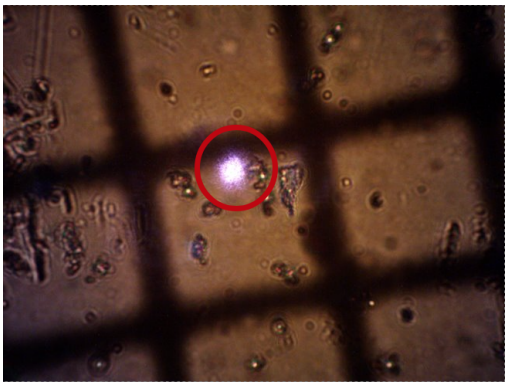

(a) Optical microscopy image of the previous laser spot: *Objective:* $20x$, *Field of view*$359,5\mu m$.

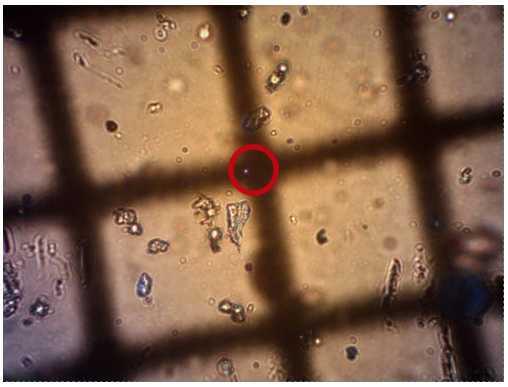

(b) Optical microscopy image of the upgraded laser spot: *Objective:* $20x$, *Field of view*$359,5\mu m$.

(**4.9**) Scanning MicroRaman images obtained with upgraded laser.

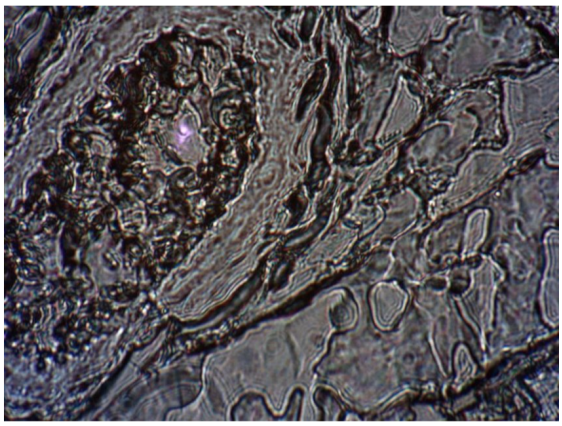

(a) Optical microscopy image: *Objective:* $100x$, *Field of view*$98\mu m$.

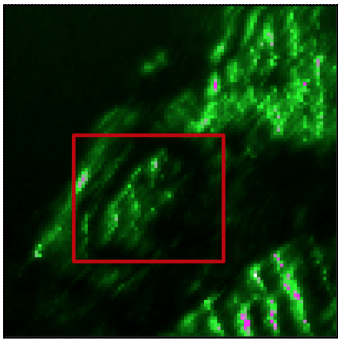

(b) Raman-Scanning map: *Laser Power* $(2mW)$, λ : $(785nm)$, *Exposure Time*: $(100ms)$ *Objective*: $(100x)$, *Scan dimension*: $200x200um$.

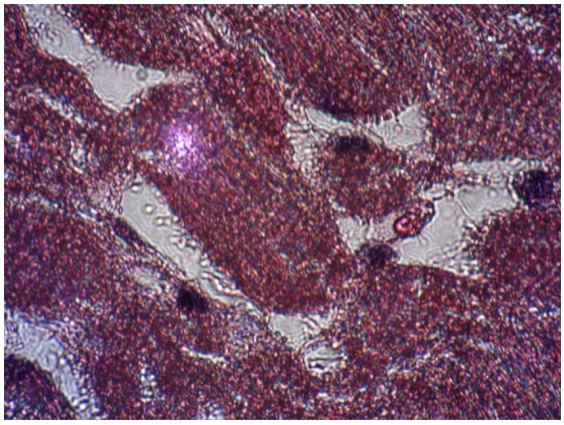

(c) Optical microscopy image: *Objective:* $100x$, *Field of view*$98um$.

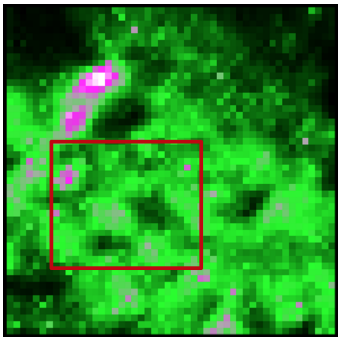

(d) Raman-Scanning map: *Laser Power* $(2mW)$, λ : $(785nm)$, *Exposure Time*: $(100ms)$ *Objective*: $(100x)$, *Scan dimension*: $200x200um$.

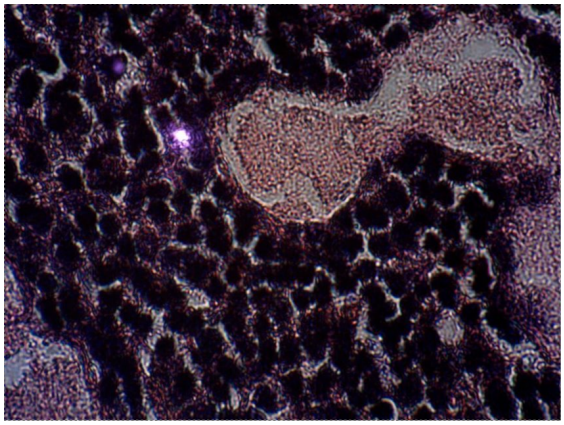

(e) Optical microscopy image: *Objective:* $100x$, *Field of view*$98um$.

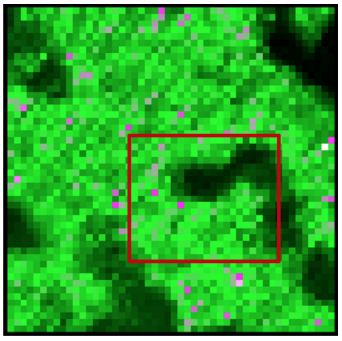

(f) Raman-Scanning map: *Laser Power* $(2mW)$, λ : $(785nm)$, *Exposure Time*: $(100ms)$ *Objective*: $(100x)$, *Scan dimension*: $200x200um$.

(**4.10**) Scanning MicroRaman mice tissue analysis.

Chapter 5

Results and Discussion

5.1 Solid-lipid nanoparticles (SLNPs morphological characterization)

In order to develop the multispectral nanoimaging system for biomedical studies, I started by analyzing the particles in solution. Photon correlation spectroscopy (PCS) analysis of the solution showed that the nanoparticles are about 60 nm in size (Fig.: refPCS). The first Step was the characterization of SLNPs through AFM. I tested different substrates to understand how best perform the technique. I considered the interactions between the substrate and the SLNPs to reduce deformation effects. I performed several preliminary tests on the substrates to find possible influences on further analysis with the SLNPs. I succeeded in taking several AFM images of the SLNPs deposited on HOPG and silicon.

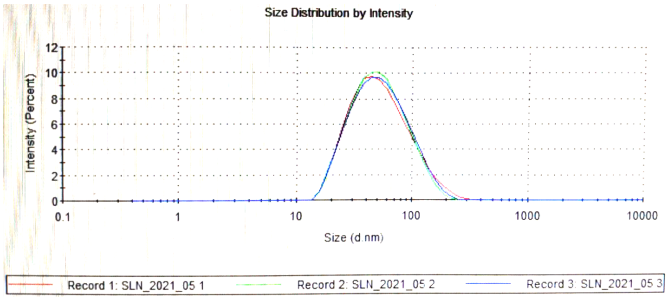

(a) PCS measurement of the SLNPs in solution.

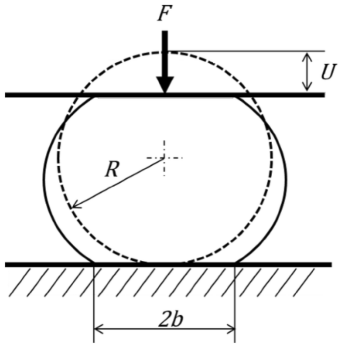

(b) Deformation of a spherical object.

(**5.1**)

The KPM analysis shows no significant differences in potential. The average height of the deposited SLNPs varies depending on the substrate and is between 10nm and 20nm. Once deposited, the SLNPs results deformed in comparison to the SLNPs in solution. This is due to surface interaction and the absence of the solution media (Fig.:5.1b). This results in a transition from a spherical to a disc-like shape, which leads to a decrease in the expected value for the height of the nanoparticles.

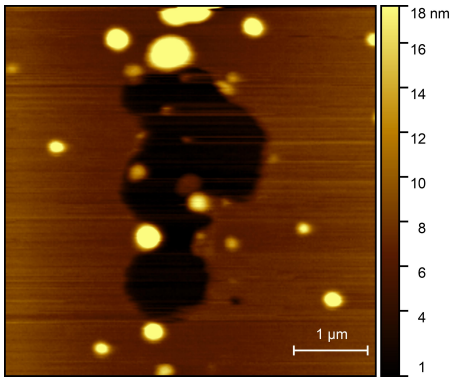

(a) AFM topographic image of SLNPs deposited on silicon. Dimension: $5umx5um$.

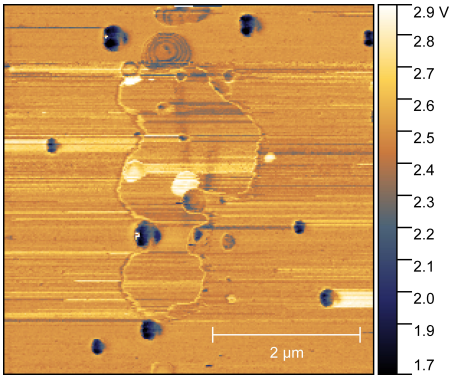

(b) AFM phase image of SLNPs deposited on silicon. Dimension: $5umx5um$.

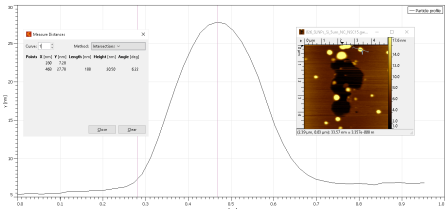

(c) Topographic profile of a single nanoparticle.

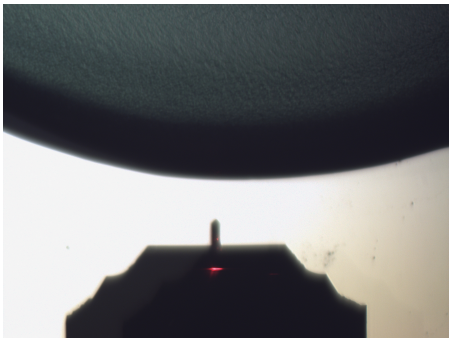

(d) Optical image.

(**5.2**) AFM analysis on the SLNPs deposited on silicon.

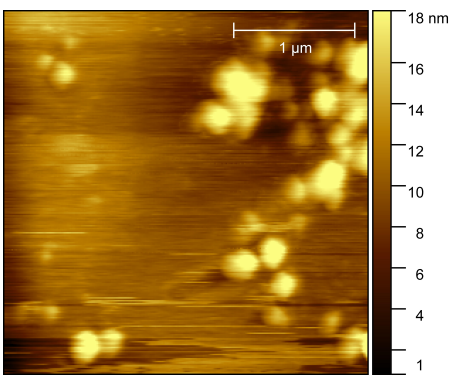

(a) AFM topographic image of SLNPs deposited on HOPG. Dimension: $3umx3um$.

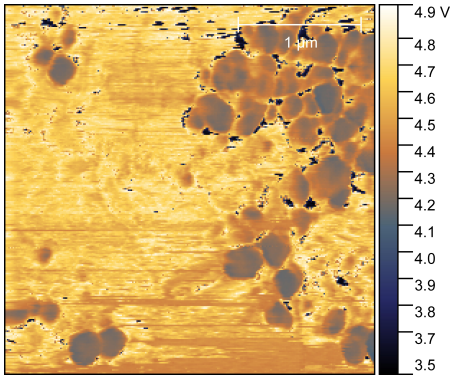

(b) AFM phase image of SLNPs deposited on HOPG. Dimension: $3umx3um$.

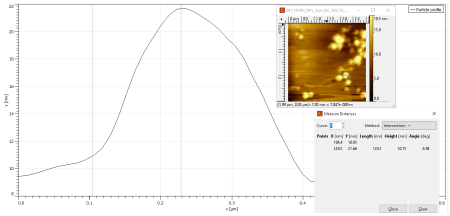

(c) Topographic profile of a single nanoparticle.

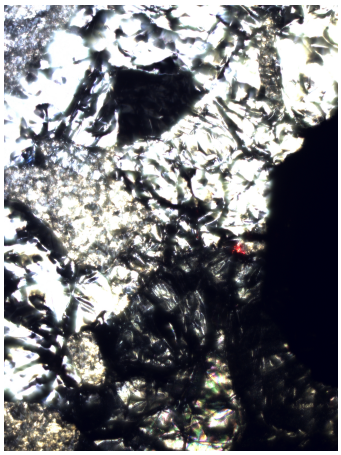

(d) Optical image.

(**5.3**) AFM analysis on the SLNPs deposited on HOPG.

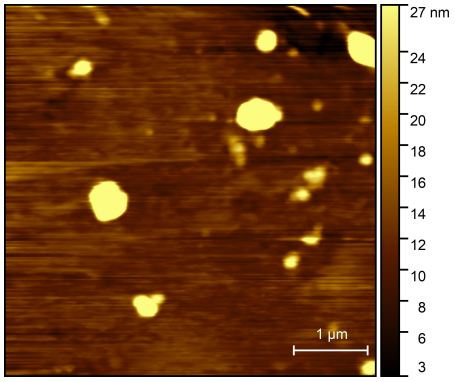

(a) AFM topographic image of SLNPs deposited on HOPG. Dimension: $5umx5um$.

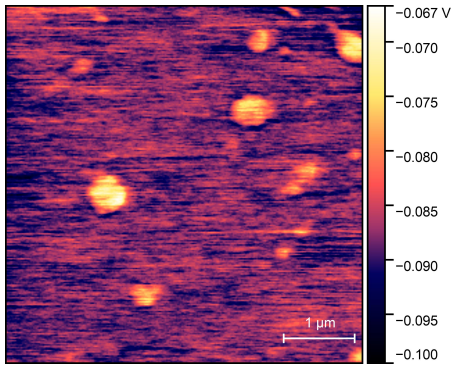

(b) AFM KPM image of SLNPs deposited on HOPG. Dimension: $5umx5um$.

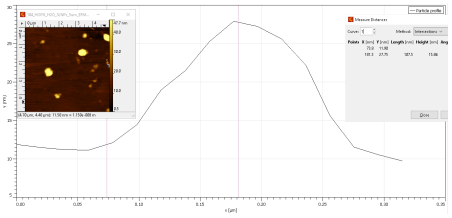

(c) Topographic profile of a single nanoparticle.

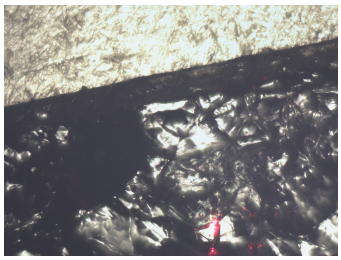

(d) Optical image.

(**5.4**) AFM KPM analysis on the SLNPs deposited on HOPG.

As expected the nanoparticles present a variation in shape. For future analysis for SLNPs in tissues I does not expect the maintenance of the spherical shape and then the same size detected in solution via PCS.

5.1.1 Gold deposition on the SLNPs

To analyse the SLNPs using STM, I decided to deposit a thin layer of gold on the SLNPs deposited on mica. Due to the nature of the SLNPs, the process resulted in the formation of a gold film with holes I associate with the destruction of the SLNPs.

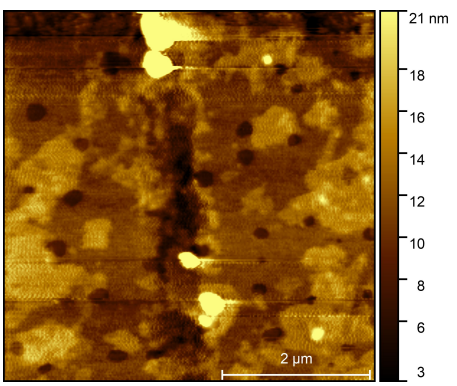

(a) AFM topographic image of SLNPs deposited on Mica and covered with a PVD Au thin film. Dimension: $5umx5um$.

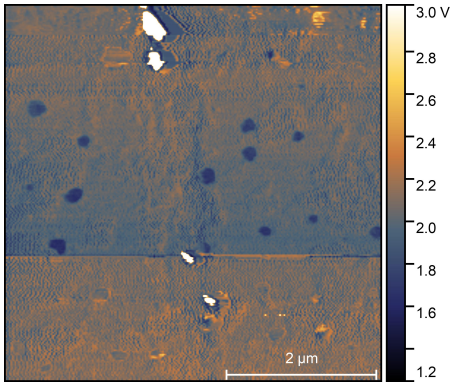

(b) AFM phase image of SLNPs deposited on Mica and covered with a PVD Au thin film.. Dimension: $5umx5um$.

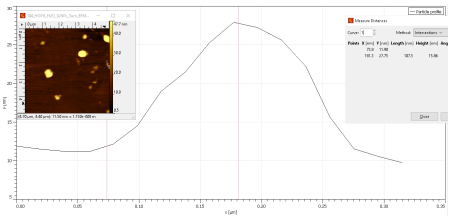

(c) Topographic profile of a single nanoparticle.

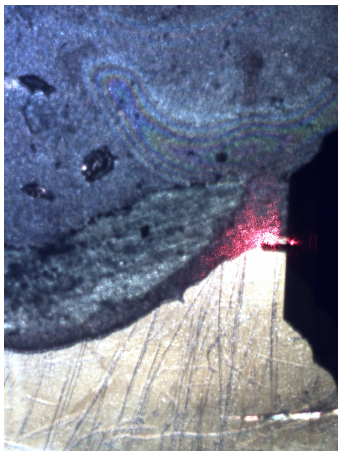

(d) Optical image.

(**5.5**) AFM KPM analysis on the SLNPs deposited on HOPG.

The holes depth range between 2nm and 3nm and depends on the deposition factor. I assume the SNLPs evaporate and prevent the gold from being deposited on the surface. Applying this technique also in biological matrices could be difficult.

5.2 Raman fingerprinting

As described in section 3.2, I have perfomed of Raman analysis, focusing on possible fingerprints of the nanoparticles or ICG.

5.2.1 ICG Scanning MicroRaman analysis

Using Raman analysis of the ICG after vacuum treatment, I was able to identify several Raman fingerprints that will be useful for future analyses.

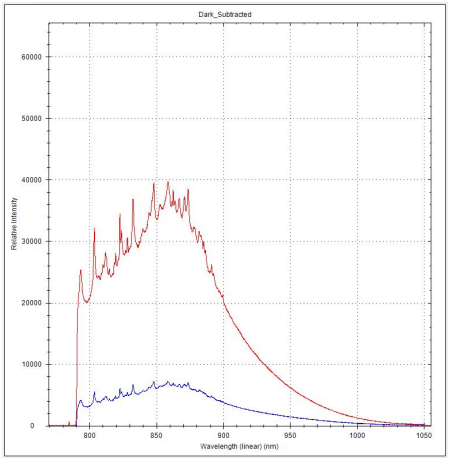

(a) Raman spectra of ICG on silicon (*Green*) and ICG on gold(*Red*): *Laser Power* ($20mW$), λ : ($785nm$), *Exposure Time*: ($1000ms$) *Objective*: ($50x$).

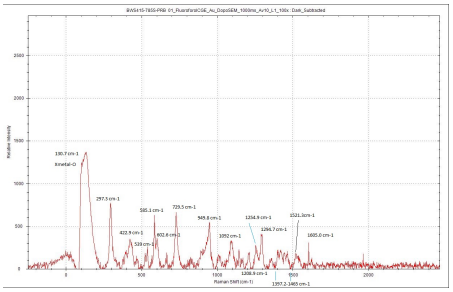

(b) Raman spectra of ICG on gold, background subtracted: *Laser Power* ($20mW$), λ : ($785nm$), *Exposure Time*: ($1000ms$) *Objective*: ($50x$).

(**5.6**) Results for the ICG Raman analysis.

As shown in the figure 5.6b, I was able to identify several peaks associated with the following vibrational models:

$wavelength(cm^{-1})$	vibrational model	
1.	$130cm^{-1}$	Xmetal-O/ Lattice Vibration
2.	$297.3cm^{-1}$	Xmetal-O/ C-C aliphatic chain
3.	$949.8cm^{-1}$	interaction between the two sulfonic acid groups
4.	$1092cm^{-1}$	C=S
5.	$1254.9cm^{-1}$	sulfonic acid
6.	$1397.2to1465cm^{-1}$	related to the nitrogen
7.	$521.3cm^{-1}$	aromatic ring
8.	$1605cm^{-1}$	aromatic hetero ring

(**5.1**) identified fingerprints for ICG on gold

The difficulty, of course, will be defining which peaks can be used in the abundance of "fingerprints" in the biological environment. Another critical point could be the area sensed by the instrument for a single spectrum acquisition. If we want to resolve a single vibrational band in the plethora of the biological environment we have to move to Raman techniques with more resolution like Tips Enhanced Raman Spectroscopy (TERS).

5.2.2 SLNPs Scanning MicroRaman analysis

With the results from the Raman analysis for the ICG dye I decided to investigate the presence of fingerprints for SLNPs-ICG system. Using the Scanning MicroRaman instrument, I created a map of the SLNPs deposited on the substrate of gold pin on silicon (Fig. 5.7b).

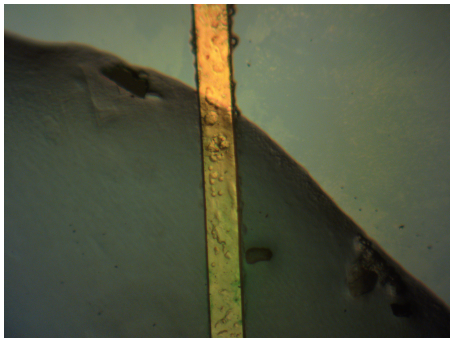

(a) Optical microscopy image: *Objective:* $20x$, *Field of view*$359,5um$

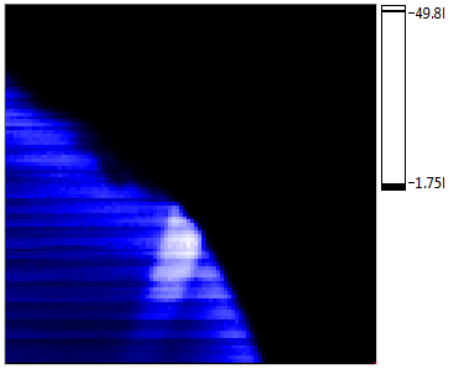

(b) Raman-Scanning map: *Laser Power* $(2mW)$, λ : $(785nm)$, *Exposure Time*: $(50ms)$ *Objective*: $(100x)$, *Scan dimension*: $400x400um$

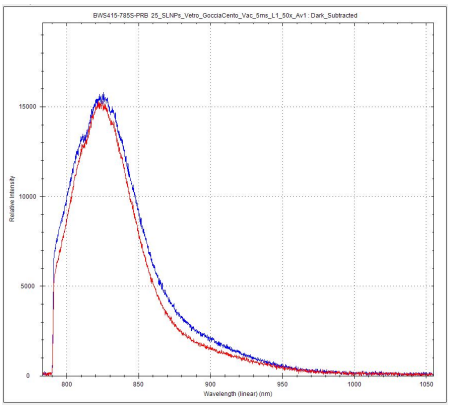

(c) Scanning MicroRaman spectra for SLNPs after deposition (*red*) and after vacuum treatement (*blue*): *Laser Power* $(2mW)$, λ : $(785nm)$, *Exposure Time*: $(5ms)$ *Objective*: $(50x)$.

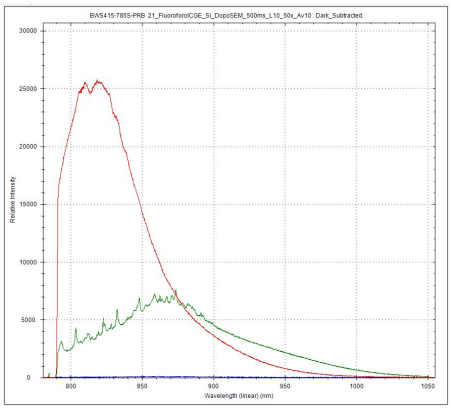

(d) ICG spectra (*green* and *blue*) compared to the SLNPs (*red*):(*Laser Power* $(2mW)$, λ : $(785nm)$, *Exposure Time*: $(5ms)$ *Objective*: $(50x)$ *blue*, *red*), (*Laser Power* $(20mW)$, λ : $(785nm)$, *Exposure Time*: $(50ms)$ *Objective*: $(50x)$ *green*).

(**5.7**) SLNPs Scanning MicroRaman analysis.

Unfortunately, the system shows a very strong fluorescence that prevents the emergence of possible fingerprints. This led us to develop a system related to the strong fluorescence of particles, with the aim of identify them within biological tissues. Analysis for possible correlation between absence of the solvent and a change in fluorescence intensity shown the fluorescence does not depend on the

solvent. After vacuum treatment, the fluorescence is maintained. Those results suggest fluorescence as a suitable phenomenon to exploit to develop a tool that can perform imaging on various substrates able to detect the SLNPs.

5.3 SNOM (near-field scanning microscopy) results

I decided to investigate the resolution of the A.P.E.Research TriA-SNOM system after the upgrades. In Fig. 5.8 and Fig. 5.9 are images of cytoplasmic extensions of oligodendrocityes. The idea was to investigate the ability of the technique with biological samples.

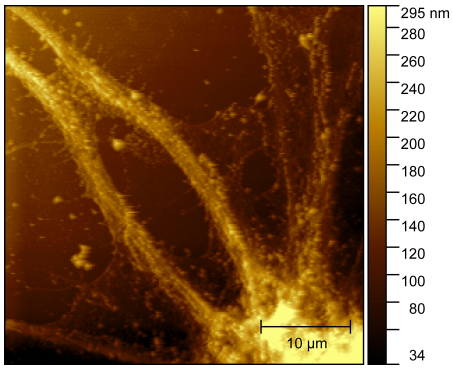

(a) SNOM topographic image of oligodendrocityes. Dimension: $40umx40um$.

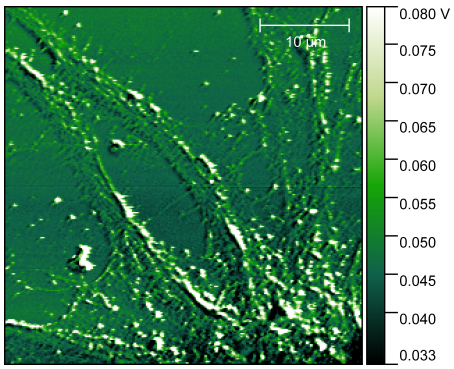

(b) SNOM reflection image of oligodendrocityes. Dimension: $40umx40um$.

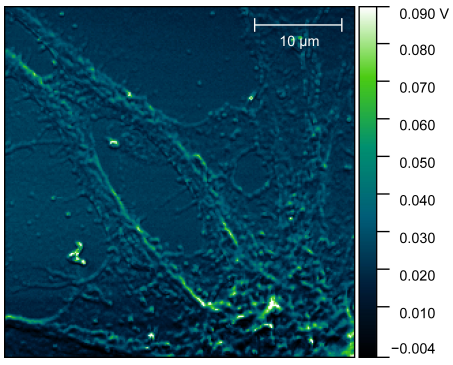

(c) SNOM trasmission image of oligodendrocityes. Dimension: $40umx40um$.

(**5.8**) SNOM analysis on oligodendrocityes.

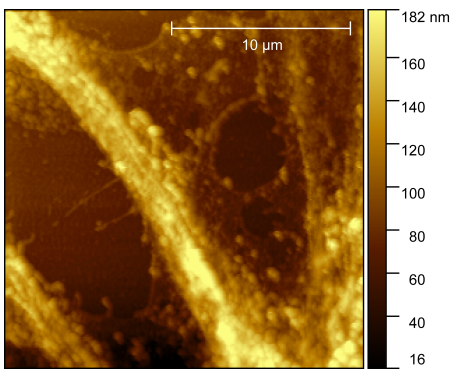

(a) SNOM topographic image of oligodendrocityes. Dimension: $20umx20um$.

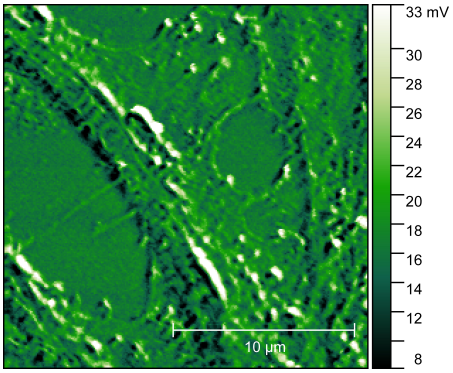

(b) SNOM reflection image of oligodendrocityes. Dimension: $20umx20um$.

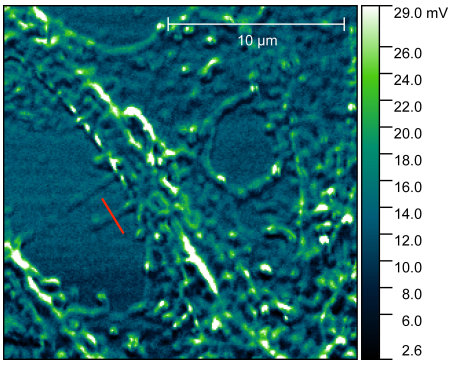

(c) SNOM trasmission image of oligodendrocityes. Dimension: $20umx20um$.

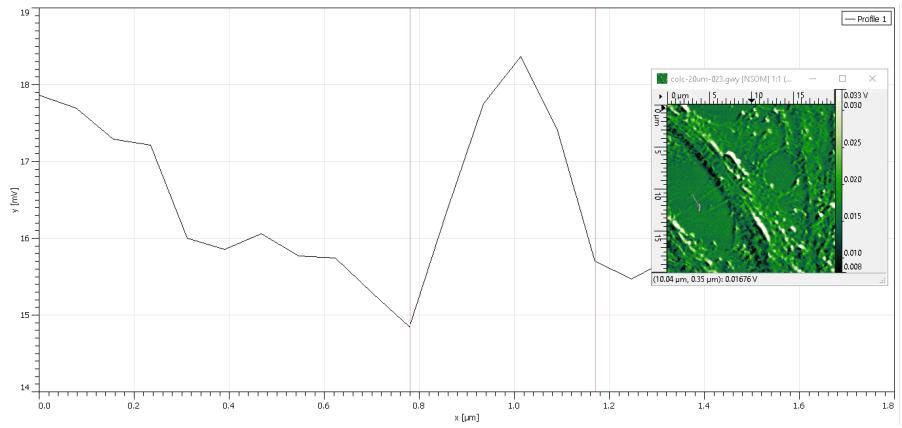

(d) Profile of a portion of the SNOM optic image.

(**5.9**) SNOM analysis on oligodendrocityes.

Conventional microscopes have a resolution of about $1um$. For SNOM, as defined in chapter 2, the resolution is related to the FWHM of a single point. To define the SNOM resolution I calculated the FWHM of a single resolved object from a SNOM-Reflection image (Fig. 5.9d). The fibre profile present a FWHM of $150nm$. This result, in order to identify fluorophores in tissues, suggest that the multispectral nanoimaging system could be able to obtain images for nanoparticles in histological samples.

Chapter 6

Conclusion

Scanning Near-fied Optical Microscopy (SNOM) has been demonstrated to be a suitable technique for the development of multispectral nanoimaging system for biomedical studies. Due to the upgrades, the time taken to perform analysis, with different wavelengths and a resolution under diffraction limit, has been drastically reduced. I started analyzing the SLNPs in solution. Photon Correlation Spectroscopy (PCS) analysis of the solution showed that the nanoparticles are about 60 nm in size. A first step see the characterization of SLNPs through Atomic force microscopy (AFM). I successfully characterised the SLNPs using atomic force microscopy (AFM). HOPG and silicon with a diluition for the SLNPs of 10^{-5} leads to the greater results. The average height of the deposited SLNPs is around $20nm$. Changes in the SLNPs dimensions from the SLNPs in solution (PCS analysis) to the condition after deposition implies the deformation of the SLNPs. The SLNPs lose the spherical shape shifting to a disk-like shape due to the change of the media and the surface interactions. For future analysis regarding SLNPs in histological samples I does not expect the SLNPs to present spherical shape. Another test I performed was the deposition of a thin film of gold on the SLNPs once deposited. No SLNPs are sensed after the deposition. Deposition of a thin film of gold on the SLNPs leads to the formation of a gold film with holes $2nm$ to $3nm$ deep, probably related to the destruction of the SLNPs. Part of this work focus on the study of SLNPs and the dye indocyanine green (ICG) through Raman spectroscopy. I used the Scanning MicroRaman sysitem provided by A.P.E. Research. To increase the resolution of the device. I modified the laser system to obtain a smaller spot. A reduction of the size of the spot lead to an increase in the resolution. Hyperspectral images of histologial section of mice tissue was successfully obtained (fig. 4.10). Histological section are fixed on slides of soda lime glass. I deceided to start studying soda-lime glass substrate to get closer to the future conditions under SLNPs will be analysed. Two conditions are investigated immediately after deposition (solvent present) and after drying (solvent evaporated). I investigate

the influence of the thickness and the different way of crystallisation of the ICG in different parts of the deposited drop. Raman analysis for nanoparticles show strong fluorescence that doesn't depend on the solvent. After vacuum treatment, the fluorescence is maintained. The analysis of ICG on gold pin deposited on silicon allowed the identification of several Raman fingerprints that will be useful for future analysis. The fingerprints are shown in table 5.5. From the results of the Scanning MicroRaman analysis I decided to use A.P.E.Research TriA-SNOM (scanning near-field optical microscopy) due to the strong fluorescence shown by the SLNPs. In collaboration with the technicians at A.P.E. Research, I've developed a system with three fibre-coupled lasers. This system makes it possible to independently modulate each laser directed at the SNOM fibre. Analysis shown no significant fluorescence arising from the optical fiber which don't contribute to the image in a way that could affect the results. Another upgrade on the SNOM allows to see the possible fluorescence of the sample through the instrument's inverted microscope. A special device has been built to switch between PMT and the inverted microscope camera. Thanks to this upgrade I was able to significantly reduce the time taken for the analysis. In my research work I also collaborate with the C.R.O. (Oncological Research Centre) in Aviano. I developed a different device starting from A.P.E. Reserach SNOM. This device is able to perform fluorescence analysis on samples that involve the presence of coverslip. Samples from the C.R.O., the ICGEB Institute and the CNR laboratories were successfully analysed. All samples were histological sections with fluorophores. I also decided to investigate the resolution of the A.P.E.Research TriA-SNOM system after the upgrades with biological samples (see Fig. 5.8, 5.9). Conventional microscopes have a resolution of about $1um$. The resolution of the image $150nm$. I successfully demonstrated that the setup is capable of performing analyses under the diffraction limit. Further upgrades can still be done both on the prototype and on the samples. For the prototype it will be interesting investigate the capability of tips enhanced Raman spectroscopy (TERS) and understand the possibility to distinguish Raman fingerprints both for the SLNPs and SLNPs on histological sections. TERS technique exploit an interesting physics phenomenon called localized surface plasmon resonance (LSPR). LSPR is related to the confined oscillation of the electrons in a metal nanostructure. Due to the strong flexibility of the prototype it could be possible upgrade it to perform TERS. The idea is use the laser source to focus a laser beam on a special AFM tip. It will be also interesting develop, both for fluorescence SNOM and Raman spectroscopy, tailored substrate able to enhance determinate wavelength exploiting the LSPR phenomenon. The preparation of Au-nanostrucutres on soda-lime glass by nanosphere lithography (NS) is a well-known process [46]. A main problem would be related to the thickness. The enhancement falls off quickly with distance from the nanostructure surface. In

conclusion, this prototype, after optimisation and appropriate development, will help to understand whether and in which tissue the NPs are taken up by the organism and thus make an important contribution to studies in the field of "drug delivery".

Bibliography

[1] V. Sanna, N. Pala, and M. Sechi, "Targeted therapy using nanotechnology: focus on cancer," *International journal of nanomedicine*, vol. 9, p. 467, 2014.

[2] J. Drbohlavova, J. Chomoucka, V. Adam, M. Ryvolova, T. Eckschlager, J. Hubalek, and R. Kizek, "Nanocarriers for anticancer drugs-new trends in nanomedicine," *Current drug metabolism*, vol. 14, no. 5, pp. 547–564, 2013.

[3] E. Blanco, A. Hsiao, A. P. Mann, M. G. Landry, F. Meric-Bernstam, and M. Ferrari, "Nanomedicine in cancer therapy: innovative trends and prospects," *Cancer science*, vol. 102, no. 7, pp. 1247–1252, 2011.

[4] D. Peer, J. M. Karp, S. Hong, O. C. Farokhzad, R. Margalit, and R. Langer, "Nanocarriers as an emerging platform for cancer therapy," *Nano-Enabled Medical Applications*, pp. 61–91, 2020.

[5] J. Conde, J. M. de la Fuente, and P. V. Baptista, "Nanomaterials for reversion of multidrug resistance in cancer: a new hope for an old idea?," 2013.

[6] P. V. Baptista, "Cancer nanotechnology-prospects for cancer diagnostics and therapy," *Current Cancer Therapy Reviews*, vol. 5, no. 2, pp. 80–88, 2009.

[7] W. H. De Jong and P. J. Borm, "Drug delivery and nanoparticles: applications and hazards," *International journal of nanomedicine*, vol. 3, no. 2, p. 133, 2008.

[8] T. Lammers, F. Kiessling, W. E. Hennink, and G. Storm, "Drug targeting to tumors: principles, pitfalls and (pre-) clinical progress," *Journal of controlled release*, vol. 161, no. 2, pp. 175–187, 2012.

[9] D. Venturoli and B. Rippe, "Ficoll and dextran vs. globular proteins as probes for testing glomerular permselectivity: effects of molecular size, shape, charge, and deformability," *American Journal of Physiology-Renal Physiology*, vol. 288, no. 4, pp. F605–F613, 2005.

[10] P. Decuzzi, R. Pasqualini, W. Arap, and M. Ferrari, "Intravascular delivery of particulate systems: does geometry really matter?," *Pharmaceutical research*, vol. 26, pp. 235–243, 2009.

[11] B. Bahrami, M. Hojjat-Farsangi, H. Mohammadi, E. Anvari, G. Ghalamfarsa, M. Yousefi, and F. Jadidi-Niaragh, "Nanoparticles and targeted drug delivery in cancer therapy," *Immunology letters*, vol. 190, pp. 64–83, 2017.

[12] H.-J. Wu, Z.-M. Wang, M. Wang, and X.-J. Wang, "Widespread long noncoding rnas as endogenous target mimics for microrna in plants," *Plant physiology*, vol. 161, no. 4, pp. 1875–1884, 2013.

[13] L. Zhou, T. Yang, J. Wang, Q. Wang, X. Lv, H. Ke, Z. Guo, J. Shen, Y. Wang, C. Xing, *et al.*, "Size-tunable gd2o3@ albumin nanoparticles conjugating chlorin e6 for magnetic resonance imaging-guided photo-induced therapy," *Theranostics*, vol. 7, no. 3, p. 764, 2017.

[14] B. Meschi Amoli, J. Trinidad, A. Hu, Y. N. Zhou, and B. Zhao, "Highly electrically conductive adhesives using silver nanoparticle (ag np)-decorated graphene: The effect of nps sintering on the electrical conductivity improvement," *Journal of Materials Science: Materials in Electronics*, vol. 26, pp. 590–600, 2015.

[15] V. A. Kamble, D. M. Jagdale, and V. J. Kadam, "Solid lipid nanoparticles as drug delivery system," *Int J Pharm Biol Sci*, vol. 1, pp. 1–9, 2010.

[16] A. Garud, D. Singh, and N. Garud, "Solid lipid nanoparticles (sln): method, characterization and applications," *International Current Pharmaceutical Journal*, vol. 1, no. 11, pp. 384–393, 2012.

[17] B. Müller, "Mikroemulsionen als neue wirksoff-trägersysteme," *Pharmazeutische Technologie: Moderne Arzneiformen. Wissenschaftliche Verlagsgesellschaft, Stuttgart*, pp. 161–168, 1998.

[18] M. R. Gasco, "Method for producing solid lipid microspheres having a narrow size distribution," Oct. 5 1993. US Patent 5,250,236.

[19] M. Gasco, "Solid lipid nanospheres from warm micro-emulsions: Improvements in sln production for more efficient drug delivery," *Pharmaceutical Technology Europe*, vol. 9, pp. 52–58, 1997.

[20] L. Boltri, T. Canal, P. Esposito, and F. Carli, "Lipid nanoparticles: evaluation of some critical formulation parameters," in *Proc Int Symp Control Release Bioact Mater*, vol. 20, pp. 346–347, 1993.

[21] S. Morel, E. Terreno, E. Ugazio, S. Aime, and M. R. Gasco, "Nmr relaxometric investigations of solid lipid nanoparticles (sln) containing gadolinium (iii) complexes," *European journal of pharmaceutics and biopharmaceutics*, vol. 45, no. 2, pp. 157–163, 1998.

[22] F. Carli, "Physical chemistry and oral absorption of the nanoparticulate systems," *Rencentre Pharmapeptides*, vol. 5, pp. 158–160, 1999.

[23] H. Hasegawa, Y. Tsukada, M. Wakabayashi, S. Nomura, T. Sasaki, Y. Nishizawa, K. Ikeda, T. Akimoto, and M. Ito, "Impact of intraoperative indocyanine green fluorescence angiography on anastomotic leakage after laparoscopic sphincter-sparing surgery for malignant rectal tumors," *International Journal of Colorectal Disease*, vol. 35, no. 3, pp. 471–480, 2020.

[24] S. Prahl *et al.*, "Optical absorption of indocyanine green (icg)," *Oregon Medical Laser Center, http://omlc. ogi. edu/spectra/icg/index. html (July 5 2011)*, 2018.

[25] S. Y. Lee, J. L. Cheng, K. M. Gehrs, J. C. Folk, E. H. Sohn, S. R. Russell, Z. Guo, M. D. Abràmoff, and I. C. Han, "Choroidal features of acute macular neuroretinopathy via optical coherence tomography angiography and correlation with serial multimodal imaging," *JAMA ophthalmology*, vol. 135, no. 11, pp. 1177–1183, 2017.

[26] G. Binnig, C. F. Quate, and C. Gerber, "Atomic force microscope," *Physical review letters*, vol. 56, no. 9, p. 930, 1986.

[27] Y. Sugimoto, P. Pou, M. Abe, P. Jelinek, R. Pérez, S. Morita, and O. Custance, "Chemical identification of individual surface atoms by atomic force microscopy," *Nature*, vol. 446, no. 7131, pp. 64–67, 2007.

[28] J. R. Ferraro, *Introductory raman spectroscopy*. Elsevier, 2003.

[29] P. Rostron, S. Gaber, and D. Gaber, "Raman spectroscopy, review," *laser*, vol. 21, p. 24, 2016.

[30] F. Ospitali, T. Sabetta, F. Tullini, M. C. Nannetti, and G. Di Lonardo, "The role of raman microspectroscopy in the study of black gloss coatings on roman pottery," *Journal of Raman Spectroscopy: An International Journal for Original Work in all Aspects of Raman Spectroscopy, Including Higher Order Processes, and also Brillouin and Rayleigh Scattering*, vol. 36, no. 1, pp. 18–23, 2005.

[31] N. D. Smith, "Fourier transform infrared spectroscopy," *Analyst*, vol. 121, p. 83N, 1996.

[32] G. M. Do Nascimento, "Introductory chapter: The multiple applications of raman spectroscopy," in *Raman Spectroscopy*, IntechOpen, 2018.

[33] D. Batchelder, "Optical techniques to characterize polymer systems," *Amsterdam: Elsevier*, p. 393, 1987.

[34] D. Batchelder and D. Bloor, "Resonance raman spectroscopy of conjugated macromolecules," *Advances in infrared and Raman spectroscopy*, vol. 11, p. 133, 1984.

[35] R. J. Clark and T. J. Dines, "Resonance raman spectroscopy, and its application to inorganic chemistry. new analytical methods (27)," *Angewandte Chemie International Edition in English*, vol. 25, no. 2, pp. 131–158, 1986.

[36] N. Kumar, W. Su, M. Veselỳ, B. M. Weckhuysen, A. J. Pollard, and A. J. Wain, "Nanoscale chemical imaging of solid–liquid interfaces using tip-enhanced raman spectroscopy," *Nanoscale*, vol. 10, no. 4, pp. 1815–1824, 2018.

[37] L. Black and A. Brooker, "Sem–sca: combined sem–raman spectrometer for analysis of opc clinker," *Advances in applied ceramics*, vol. 106, no. 6, pp. 327–334, 2007.

[38] G. M. do Nascimento, V. R. Constantino, and M. L. Temperini, "Spectroscopic characterization of doped poly (benzidine) and its nanocomposite with cationic clay," *The Journal of Physical Chemistry B*, vol. 108, no. 18, pp. 5564–5571, 2004.

[39] G. M. Do Nascimento, V. R. Constantino, R. Landers, and M. L. Temperini, "Aniline polymerization into montmorillonite clay: a spectroscopic investigation of the intercalated conducting polymer," *Macromolecules*, vol. 37, no. 25, pp. 9373–9385, 2004.

[40] G. M. do Nascimento and M. L. Temperini, "Structure of polyaniline formed in different inorganic porous materials: A spectroscopic study," *European Polymer Journal*, vol. 44, no. 11, pp. 3501–3511, 2008.

[41] R. H. Sestrem, D. C. Ferreira, R. Landers, M. L. Temperini, and G. M. do Nascimento, "Synthesis and spectroscopic characterization of polymer and oligomers of ortho-phenylenediamine," *European polymer journal*, vol. 46, no. 3, pp. 484–493, 2010.

[42] G. M. do Nascimento, R. C. de Oliveira, N. A. Pradie, P. R. G. Lins, P. R. Worfel, G. R. Martinez, P. Di Mascio, M. S. Dresselhaus, and P. Corio, "Single-wall carbon nanotubes modified with organic dyes: Synthesis, characterization and potential cytotoxic effects," *Journal of Photochemistry and Photobiology A: Chemistry*, vol. 211, no. 2-3, pp. 99–107, 2010.

[43] N. F. van Hulst, J.-A. Veerman, M. F. Garcıa-Parajó, and L. Kuipers, "Analysis of individual (macro) molecules and proteins using near-field optics," *The Journal of Chemical Physics*, vol. 112, no. 18, pp. 7799–7810, 2000.

[44] E. Betzig, A. Lewis, A. Harootunian, M. Isaacson, and E. Kratschmer, "Near field scanning optical microscopy (nsom): development and biophysical applications," *Biophysical journal*, vol. 49, no. 1, pp. 269–279, 1986.

[45] K. K. Sharma, *Optics: principles and applications*. Elsevier, 2006.

[46] A. J. Haes and R. P. Van Duyne, "A nanoscale optical biosensor: sensitivity and selectivity of an approach based on the localized surface plasmon resonance spectroscopy of triangular silver nanoparticles," *Journal of the American Chemical Society*, vol. 124, no. 35, pp. 10596–10604, 2002.